

This is a pre-print version of the paper. Please cite the final version of the paper:

G. Di Martino, A. Di Simone, A. Iodice, D. Riccio “Bistatic Scattering From Anisotropic Rough Surfaces via a Closed-Form Two-Scale Model”, *IEEE Trans. Geosci. Remote Sens.*, vol. 59, no. 5, pp. 3656-3671, May 2021.
DOI: [TGRS.2020.3021784](https://doi.org/10.1109/TGRS.2020.3021784).

IEEE Copyright notice. © 2020 IEEE. Personal use of this material is permitted. Permission from IEEE must be obtained for all other uses, in any current or future media, including reprinting/republishing this material for advertising or promotional purposes, creating new collective works, for resale or redistribution to servers or lists, or reuse of any copyrighted component of this work in other works.

Bistatic Scattering From Anisotropic Rough Surfaces via a Closed-Form Two-Scale Model

Gerardo Di Martino¹, Senior Member, IEEE, Alessio Di Simone², Member, IEEE,
Antonio Iodice³, Senior Member, IEEE, and Daniele Riccio⁴, Fellow, IEEE

Abstract—Bistatic radars have been a topic of increasing interest in recent years, thanks to the introduction of new bistatic (and multistatic) configurations, including those based on the opportunistic exploitation of global navigation satellite systems (GNSSs). The research on bistatic electromagnetic scattering models plays an important role in the analysis of these systems, in their simulation, and in the prediction of their performance. The two-scale model (TSM) is a widely used approach for the computation of scattering from rough surfaces, since it is able to account for depolarization effects due to surface tilting. However, in its original formulation, it requires a computationally intensive numerical integration, in order to perform appropriate average over surface random slopes. To overcome this limitation, a closed-form polarimetric TSM (PTSM) was developed, which has been also recently extended to the case of anisotropic rough surfaces (A-PTSM), with a focus on the sea surface. The A-PTSM can be efficiently used to compute the backscattering from anisotropic rough surfaces and can support the development and analysis of monostatic radar missions. In order to extend its scope to the general case of bistatic and multistatic configurations, in this article, we extend the A-PTSM to the case of bistatic electromagnetic scattering, presenting the evaluation of all the elements of the bistatic polarimetric covariance matrix. Due to the relevance of circularly polarized signals in opportunistic GNSS reflectometry applications, both the linear and the circular polarization bases are considered. The behavior of the obtained elements is discussed, and simplified expressions of the elements of the covariance matrix are provided for the case of scattering within the incidence plane. Relevant numerical examples are provided and compared to those obtained by the more refined, but more computationally intensive, second-order small-slope approximation (SSA2) method. In the examples, we consider both a wind-driven sea surface and a tilled soil, and both L-band and X-band frequencies. However, the presented method can be used at all frequencies of interest for microwave remote sensing and for all observation geometries, except for near grazing incidence and/or scattering.

Index Terms—Bistatic scattering, scattering from rough surfaces, polarimetry, sea surface.

I. INTRODUCTION

THE prediction of bistatic electromagnetic scattering has been widely investigated in the last decade, due to the

Manuscript received May 27, 2020; revised July 22, 2020 and August 31, 2020; accepted September 1, 2020. This work was supported by the Italian Ministry of University and Research (MIUR) through PON “FORCE—Volo in formazione di assemblati di CubeSat per l’osservazione della Terra.” (Corresponding author: Gerardo Di Martino.)

The authors are with the Dipartimento di Ingegneria Elettrica e delle Tecnologie dell’Informazione, Università degli Studi di Napoli Federico II, 80125 Naples, Italy (e-mail: gerardo.dimartino@unina.it; alessio.disimone@unina.it; iodice@unina.it; daniele.riccio@unina.it).

Color versions of one or more of the figures in this article are available online at <http://ieeexplore.ieee.org>.

Digital Object Identifier 10.1109/TGRS.2020.3021784

increasing interest in bistatic (and multistatic) radar configurations [1]–[11]. In this context, an important role is played by systems based on the opportunistic exploitation of global navigation satellite system (GNSS) signals [6]–[11]. As a matter of fact, the scattered signals bear meaningful information about the geophysical quantities characterizing the observed surface [10]–[14]. Therefore, the development of appropriate electromagnetic models is of paramount importance in supporting the extraction of information from the measured data [5], [11], [12], [14]. In particular, in order to effectively describe the GNSS signals, these models must be able to provide a complete characterization of circularly polarized returns, which can be obtained through an appropriate change in polarization basis once a fully polarimetric characterization in the linear basis is available [15]. As a matter of fact, the key point in fully polarimetric scattering modeling regards the inclusion of the cross-polarized components (also for scattering directions within the plane of incidence) and the accurate evaluation of the off-diagonal terms of the covariance matrix [15].

In the last 50 years, the problem of the evaluation of scattering from a rough surface including cross-polarization has been approached considering several different theoretical models [14], [16]–[29]. One of the most widely used is the two-scale model (TSM), also known as composite model (CM) [16], [17], which has gained particular attention for sea scattering computation [19], [21], [23], [24], [28], [30]–[32]. The TSM is based on a two-scale description of the rough surface: a small-scale roughness, with horizontal scale of the order of the wavelength and vertical deviations much smaller than the wavelength, is superimposed over a large-scale roughness, with horizontal scale much larger than the wavelength and vertical deviations of the order of the wavelength or higher. For each roughness scale, an appropriate scattering model is adopted: in particular, scattering from large-scale roughness is evaluated by using the geometrical optics (GO) approximation, whereas scattering from the small-scale roughness is usually computed by evaluating the scattering from a randomly tilted rough facet via the small perturbation method (SPM). In order to properly account for cross-polarization and depolarization effects, it is necessary to average the elements of the small-scale scattering covariance matrix over the facet random slopes, whose statistical distribution follows the large-scale surface slope probability density function (pdf). The GO contribution is dominant in nearly specular directions and its polarimetric covariance matrix elements depend on the large-scale surface slope pdf. Conversely, the scattering from small-scale roughness is dominant for intermediate incidence

angles in far-from-specular scattering directions and is mainly dependent on the small-scale roughness power spectral density (PSD).

The original formulation of the TSM requires the numerical evaluation of the integral accounting for the averaging over surface slopes, so that the model does not provide closed-form expressions for the elements of the polarimetric covariance matrix [16], [17], [19], [24], [30]. This can be considered one of the main drawbacks of the standard TSM, considerably limiting its application whenever wide-area real-time monitoring is of interest. However, in recent years, a closed-form formulation of the TSM, the polarimetric TSM (PTSM), was developed [25], [28]. The PTSM expressions are obtained expanding to the second order the tilted-facet SPM covariance matrix elements with respect to large-scale surface slopes and are, therefore, suitable for moderate large-scale surface slopes [25], [28]. In its original formulation, the PTSM was introduced to model the backscattering from isotropic rough soils, in order to be used in support of soil moisture retrieval procedures from polarimetric synthetic aperture radar (SAR) data [25], [27]. However, the hypothesis of isotropic surfaces may be not adequate in a wide set of physical situations, ranging from tilled agricultural soils [29], [33] to the wind-driven sea surface [34]–[36]. Consequently, very recently an extension to the case of anisotropic rough surfaces, the anisotropic (or Advanced) PTSM (A-PTSM), has been presented [28]. In particular, in [28], the backscattering from a wind-driven sea surface has been extensively discussed, both in the linear and circular polarimetric scattering basis.

Electromagnetic models for the evaluation of bistatic scattering from rough surfaces represent an important tool for the extraction of value-added information from existing or upcoming bistatic (and multistatic) radar missions. In this context, GNSS reflectometry (GNSS-R) applications are certainly one of the main driving factors [11], even if the development of radar constellations, possibly made up of small satellites [10], is also drawing significant attention [3]–[5]. In this article, we extend the A-PTSM to the bistatic case, deriving the bistatic A-PTSM (BA-PTSM). In particular, the expressions of all the elements of the polarimetric covariance matrix of an anisotropic rough surface are provided in both linear and circular polarization. Moreover, for scattering directions lying within the incidence plane particularly simple closed-form expressions are obtained, which can better support the physical interpretation of the scattering process.

A drawback of the TSM, which is also inherited by the A-PTSM, consists in the underestimation of depolarization effects: indeed, only depolarization due to facet tilting is taken into account, whereas depolarization due to multiple scattering is ignored [18], [26]. Conversely, the second-order small-slope approximation (SSA2) also accounts for multiple scattering [18], [26], but, as a consequence, it requires a computationally intensive numerical evaluation of fourfold integrals. In [26] and [28], it was shown that, as expected, the higher accuracy of SSA2 mainly affects the cross-polarized terms, which the TSM and A-PTSM underestimate by 2–4 dB with respect to the SSA2 value. In this article, we compare the results obtained with our BA-PTSM with the SSA2 ones

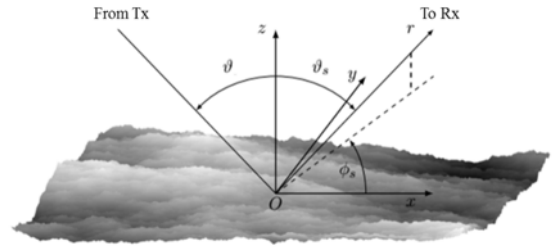


Fig. 1. Geometry of the problem and coordinate system.

reported in [26]. However, we present a wider set of graphs and examples than those shown in [26], in order to provide an analysis of the dependencies of the scattering behavior from the main scattering parameters.

II. SURFACE DESCRIPTION

The proposed method can be applied to any anisotropic randomly rough surface. However, in Section IV, we will focus on the two scenarios of wind-driven sea surfaces and tilled agricultural soils.

A. General Anisotropic Randomly Rough Surface

The geometry of the problem, with the employed coordinate system, is depicted in Fig. 1. The xy plane coincides with the mean plane of the rough surface, with the x -axis lying in the incidence plane (i.e., the plane defined by the z -axis and the direction of propagation of the incident wave), whereas the scattering plane is defined by the z -axis and the direction of propagation of the scattered wave). The components of the electromagnetic wavenumber vector \mathbf{k}_i of the incident wave are

$$\begin{aligned} k_{ix} &= k \sin \vartheta_i \\ k_{iy} &= 0 \\ k_{iz} &= -k \cos \vartheta_i \end{aligned} \quad (1)$$

where ϑ_i is the incidence angle, and k is the electromagnetic wavenumber, and the components of the electromagnetic wavenumber vector \mathbf{k}_s of the scattered wave are

$$\begin{aligned} k_{sx} &= k \sin \vartheta_s \cos \varphi_s \\ k_{sy} &= k \sin \vartheta_s \sin \varphi_s \\ k_{sz} &= k \cos \vartheta_s \end{aligned} \quad (2)$$

where ϑ_s and φ_s are the zenith and azimuth scattering angles, respectively.

In our version of the TSM, the overall scattering surface is modeled as a collection of randomly rough facets, whose roughness is the small-scale roughness; the facets are randomly tilted according to the slope of the large-scale roughness. In order to implement the TSM, we must specify the PSD of the small-scale roughness height and the pdf of the large-scale roughness slopes. With regard to the former, it can be expressed in general as

$$W_{2D}(\kappa_x, \kappa_y) = W_{2D}(\kappa, \varphi) \quad (3)$$

where $\boldsymbol{\kappa} = \kappa_x \hat{\mathbf{i}}_x + \kappa_y \hat{\mathbf{i}}_y$ is the surface wavenumber vector, $\kappa = (\kappa_x^2 + \kappa_y^2)^{1/2}$ is its modulus, and $\varphi = \arctan(\kappa_y/\kappa_x)$ is the angle between its direction and the x -axis. Although any PSD can be considered by our approach, we assume that, for surface wavenumbers around the Bragg resonant one $\bar{\kappa}$, with

$$\bar{\boldsymbol{\kappa}} = (-k \sin \vartheta_s \cos \varphi_s + k \sin \vartheta_1) \hat{\mathbf{i}}_x + (-k \sin \vartheta_s \sin \varphi_s) \hat{\mathbf{i}}_y \quad (4)$$

it can be approximated as

$$W_{2D}(\boldsymbol{\kappa}, \varphi) \cong W(\kappa) \Phi(\varphi) \quad (5)$$

with

$$W(\kappa) = \frac{S_0}{\kappa^\alpha} \quad (6)$$

and

$$\Phi(\varphi) = 1 + \Delta \cos[2(\varphi_0 - \varphi)] \quad (7)$$

where α , S_0 , Δ , and φ_0 are the parameters characterizing the anisotropic surface small-scale roughness. In fact, as it will be better explained in Section III-C, and similar to what we did in the monostatic case in [28], in scattering evaluations, we will use (5)–(7) for the computation of higher order terms of power series expansions. However, for the dominant terms, we will use the exact PSD expressions, evaluated at the Bragg resonant wavenumber.

With regard to the large-scale roughness, we assume that its surface slopes s_X and s_Y along the X - and Y -axes of a preferential reference system are Gaussian zero-mean independent random variables with the variances σ_X^2 and σ_Y^2 . Under this assumption, it is easy to show [28] that surface slopes s_x and s_y along the x - and y -directions are zero-mean jointly Gaussian random variables with the variances

$$\begin{aligned} \sigma_x^2 &= \sigma_X^2 \cos^2 \psi + \sigma_Y^2 \sin^2 \psi \\ &= \frac{\sigma_X^2 + \sigma_Y^2}{2} \left[1 + \frac{\sigma_X^2 - \sigma_Y^2}{\sigma_X^2 + \sigma_Y^2} \cos 2\psi \right] \\ \sigma_y^2 &= \sigma_Y^2 \cos^2 \psi + \sigma_X^2 \sin^2 \psi \\ &= \frac{\sigma_X^2 + \sigma_Y^2}{2} \left[1 - \frac{\sigma_X^2 - \sigma_Y^2}{\sigma_X^2 + \sigma_Y^2} \cos 2\psi \right] \end{aligned} \quad (8)$$

and correlation coefficient

$$\rho = \frac{1}{2} \sin 2\psi \frac{\sigma_Y^2 - \sigma_X^2}{\sigma_x \sigma_y} \quad (9)$$

where ψ is the angle between the X - and x -axes (i.e., the angle of rotation of the X - Y reference system with respect to the x - y one).

It is useful to notice that, by using (8) and (9), after some simple algebra we get

$$\sigma_x^2 \sigma_y^2 (1 - \rho^2) = \sigma_X^2 \sigma_Y^2 \quad (10)$$

so that this quantity is independent of the angle ψ .

Finally, we recall that the separation between small-scale roughness and large-scale roughness is provided by a cutoff wavenumber κ_{cut} of the order of (but smaller than) the electromagnetic wavenumber k . The choice of κ_{cut} has a certain degree of arbitrariness. However, as it will be made clearer in the following, the results of our approach are substantially independent of this choice.

B. Wind-Driven Sea Surfaces

In the case of wind-driven sea surfaces, by following the approach of [28], for the small-scale roughness PSD, we use the high-frequency part of the Elfouhaily spectrum [34]. Its detailed expression can be found in [28, eqs. (2)–(8)]. Around the Bragg resonance wavenumber, this PSD is well approximated by (5)–(7) in which $\alpha = 3.5$, and S_0 and Δ depend on wind speed according to the relations detailed in [28], so that Δ is usually much smaller than unity, and $\varphi_0 = \varphi_w$, where φ_w is the angle between the wind direction and the x -axis. We stress again that in scattering evaluations, we will use (5)–(7) only for the computation of higher order terms of power series expansions; in this sea surface case, for the dominant terms, we will use the exact expressions of the Elfouhaily spectrum, as reported in [28] and [34].

With regard to large-scale roughness, in this case, X and Y axes are along the upwind and crosswind directions, respectively, so that $\psi = \varphi_w$, and σ_X^2 and σ_Y^2 are the upwind and crosswind variances σ_{up}^2 and σ_{cross}^2 , respectively [35]. The latter can be computed according to the approach of [28] as

$$\sigma_{X,Y}^2 = \sigma_{\text{up,cross}}^2 \cong \sigma_{\text{up0,cross0}}^2 + \frac{S_0}{2\pi} \left(1 \pm \frac{\Delta}{2} \right) (\sqrt{\kappa_{\text{cut}}} - \sqrt{\kappa_{\text{cut0}}}) \quad (11)$$

where $\sigma_{\text{up0,cross0}}^2$ are the wind-speed-dependent values obtained by using the semiempirical evaluation of [36] that holds at the frequency of 1.5 GHz, κ_{cut} is the cutoff wavenumber at the considered incident electromagnetic wave frequency, and κ_{cut0} is the cutoff wavenumber at 1.5 GHz. Note that the bulk of the evaluation in (11) is based on the semiempirical values $\sigma_{\text{up0,cross0}}^2$ that do not depend on the choice of κ_{cut} . The remaining term represents a small correction to account for a microwave frequency different from 1.5 GHz, and it only slightly depends on the cutoff wavenumber, due to the difference that appears in the rightmost parenthesis of (11). Accordingly, the slope variances in (11) are substantially independent of the choice of the cutoff wavenumber. For a wider discussion of this issue, and for the expressions of $\sigma_{\text{up0,cross0}}^2$, the reader is referred to [28]. In this work, we will use $\kappa_{\text{cut}} = 3k(\sigma_X \sigma_Y)^{1/2}$. This choice will be justified in Section III-D.

In summary, wind speed and direction completely characterize the wind-driven sea surface geometry and are the input parameters for the surface model, together with the sea complex relative permittivity.

C. Tilled Agricultural Soil

For tilled agricultural fields, by following an approach similar to the one of [29], we assume that the small-scale roughness is statistically isotropic, so that the anisotropy is entirely due to the large-scale roughness. However, at the variance with [29], we model the soil small-scale roughness as a band-limited 2D fractional Brownian motion (fBm) process [25], whose PSD is given by (5)–(7), in which $\Delta = 0$ (so that φ_0 is meaningless), S_0 is directly proportional to the small-scale roughness height variance via a dimensional facet-size-dependent constant the expression of which is reported in [37], and $\alpha = 2 + 2H$, with

H being the fBm Hurst coefficient. The latter can span from 0 to 1, but, for most natural soil surfaces, it is in the range from 0.6 to 0.8 [37].

With regard to the large-scale roughness, we assume that the Y -axis is along the plowing direction, and the X -axis is perpendicular to it, so that σ_X^2 is significantly larger than σ_Y^2 . We consider these variances as independent inputs of our method.

In summary, the input parameters of the tilled soil model are S_0 , H , ψ , σ_X^2 , and σ_Y^2 , together with the soil complex relative permittivity.

III. BISTATIC ANISOTROPIC PTSM

In the TSM, the elements of the bistatic polarimetric covariance matrix, $R_{pq,rs}$, are evaluated as the sum of the large-scale roughness contribution, $R_{pq,rs}^{\text{GO}}$, computed via the GO, and the small-scale roughness contribution, $\langle R_{pq,rs}^{\text{SPM}} \rangle_{s_x, s_y}$, computed as the SPM scattering from a tilted rough facet, averaged over the large-scale surface slopes

$$R_{pq,rs} = R_{pq,rs}^{\text{GO}} + \langle R_{pq,rs}^{\text{SPM}} \rangle_{s_x, s_y} \quad (12)$$

where the subscripts p , q , r , and s may each stand for h (horizontal polarization) or v (vertical polarization), and the symbol $\langle \cdot \rangle_{s_x, s_y}$ represents the statistical mean with respect to the random variables s_x and s_y . Note that $R_{pq,pq}$ is the bistatic normalized radar cross section (NRCS) σ_{pq}^0 at pq polarization and that the covariance matrix is Hermitian, i.e., $R_{rs,pq} = R_{pq,rs}^*$, where $*$ stands for complex conjugate. We will use the ‘‘backscatter alignment’’ (BSA) convention [15].

A. GO Scattering From the Large-Scale Roughness

By recalling the results of [38]–[40] and using the expression of the pdf of jointly Gaussian random variables, it can be shown that GO leads to the following formulas for the elements of the polarimetric covariance matrix of the large-scale roughness contribution:

$$R_{pq,rs}^{\text{GO}} = \frac{S_{pq} S_{rs}^*}{2\sigma_x \sigma_y \sqrt{1 - \rho^2} (\cos \vartheta_i + \cos \vartheta_s)^4} \times \exp \left\{ - \frac{\sigma_x^2 \bar{\kappa}_y^2 + \sigma_y^2 \bar{\kappa}_x^2 - 2\sigma_x \sigma_y \rho \bar{\kappa}_x \bar{\kappa}_y}{2k^2 \sigma_x^2 \sigma_y^2 (1 - \rho^2) (\cos \vartheta_i + \cos \vartheta_s)^2} \right\} \quad (13)$$

where $\bar{\kappa}_x$ and $\bar{\kappa}_y$ are the x and y components of $\bar{\kappa}$, see (4)

$$\begin{aligned} S_{hh} &= \frac{\Gamma_h(\vartheta_0) T T' - \Gamma_v(\vartheta_0) U U'}{\sin^2 \vartheta_0} \\ S_{vh} &= \frac{\Gamma_h(\vartheta_0) T' U' + \Gamma_v(\vartheta_0) T U}{\sin^2 \vartheta_0} \\ S_{hv} &= - \frac{\Gamma_h(\vartheta_0) T U + \Gamma_v(\vartheta_0) T' U'}{\sin^2 \vartheta_0} \\ S_{vv} &= - \frac{\Gamma_h(\vartheta_0) U U' - \Gamma_v(\vartheta_0) T T'}{\sin^2 \vartheta_0} \end{aligned} \quad (14)$$

$$\begin{aligned} T &= \sin \vartheta_i \cos \vartheta_s + \cos \vartheta_i \sin \vartheta_s \cos \varphi_s \\ T' &= \sin \vartheta_s \cos \vartheta_i + \cos \vartheta_s \sin \vartheta_i \cos \varphi_s \\ U &= - \sin \vartheta_i \sin \varphi_s \\ U' &= - \sin \vartheta_s \sin \varphi_s \end{aligned} \quad (15)$$

$$\vartheta_0 = \frac{1}{2} \arccos(-\sin \vartheta_i \sin \vartheta_s \cos \varphi_s + \cos \vartheta_i \cos \vartheta_s) \quad (16)$$

$$\begin{aligned} \Gamma_h(\vartheta_0) &= \frac{\cos \vartheta_0 - \sqrt{\varepsilon - \sin^2 \vartheta_0}}{\cos \vartheta_0 + \sqrt{\varepsilon - \sin^2 \vartheta_0}} \\ \Gamma_v(\vartheta_0) &= - \frac{\varepsilon \cos \vartheta_0 - \sqrt{\varepsilon - \sin^2 \vartheta_0}}{\varepsilon \cos \vartheta_0 + \sqrt{\varepsilon - \sin^2 \vartheta_0}} \end{aligned} \quad (17)$$

with ε being the complex relative permittivity of the scattering surface, and $\Gamma_{h,v}$ are the Fresnel reflection coefficients.

Due to the presence of the exponential factor in (13), in general, the GO contribution attains its maximum in the specular direction, identified by $\vartheta_s = \vartheta_i$ and $\varphi_s = 0$: in fact, in this case, $\bar{\kappa} = 0$ and the argument of the exponential in (13) vanishes. When the scattering direction departs from the specular one, the argument of the exponential increases and the exponential rapidly decreases. Therefore, the GO contribution is nonnegligible only in a narrow solid angle around the specular direction, such that the numerator of the exponential argument is smaller than a few times the denominator.

In addition, for scattering directions lying within the incidence plane (‘‘in-plane scattering’’), i.e., for $\varphi_s = n\pi$, with $n = 0, 1$, we have $\cos \varphi_s = (-1)^n$, $\sin \varphi_s = 0$, so that (14)–(16) become

$$\begin{aligned} \vartheta_0 &= \frac{|\vartheta_i + (-1)^n \vartheta_s|}{2} \\ T &= \sin[\vartheta_i + (-1)^n \vartheta_s] = -T' \\ U &= U' = 0 \\ S_{pp} &= \frac{-\sin^2 2\vartheta_0 \Gamma_p(\vartheta_0)}{\sin^2 \vartheta_0} = -(2 \cos \vartheta_0)^2 \Gamma_p(\vartheta_0) \\ S_{vh} &= S_{hv} = 0. \end{aligned} \quad (18)$$

Equation (4) reduces to $\bar{\kappa}_x = k[\sin \vartheta_i - (-1)^n \sin \vartheta_s]$, $\bar{\kappa}_y = 0$, and the GO expression simplifies as

$$R_{pq,rs}^{\text{GO}} = \begin{cases} \frac{(2 \cos \vartheta_0)^4 \Gamma_p(\vartheta_0) \Gamma_r^*(\vartheta_0)}{2\sigma_x \sigma_y \sqrt{1 - \rho^2} (\cos \vartheta_i + \cos \vartheta_s)^4} \exp \left\{ - \frac{[\sin \vartheta_i - (-1)^n \sin \vartheta_s]^2}{2\sigma_x^2 (1 - \rho^2) (\cos \vartheta_i + \cos \vartheta_s)^2} \right\} & \text{if, } p = q \text{ and } r = s \\ 0, & \text{otherwise.} \end{cases} \quad (19)$$

Note that, in this case of in-plane scattering, no depolarization is present in the GO contribution.

Finally, it can be verified that in the backscattering direction, identified by $\vartheta_s = \vartheta_i$ and $\varphi_s = \pi$, (18) and (19) lead to the GO expression reported in [28].

As it is well known, GO, and then (13) and (19), is not accurate at small incidence and/or scattering grazing angles. In addition, it is not accurate at scattering directions very far from the specular one. However, in all these conditions, the GO contribution in (12) is negligible with respect to the SPM one, so that we do not need to worry about these validity limits of (13) and (19).

B. SPM Scattering From a Tilted Rough Facet

Starting from the expressions of the SPM bistatic covariance matrix elements of a planar rough surface [37], [38], the SPM bistatic covariance matrix elements of the tilted facet can be expressed in the facet local reference system, i.e., in terms of the local incidence ϑ_{li} and scattering ϑ_{ls} , φ_{ls} angles, and rotation angles β_i and β_s of the incidence and scattering planes (local incidence and scattering planes being defined by the normal to the facet and by the direction of propagation of the incident and scattered waves, respectively) as

$$R_{pq,rs}^{\text{SPM}} = \frac{4}{\pi} k^4 \cos^2 \vartheta_{li} \cos^2 \vartheta_{ls} \chi_{pq} \chi_{rs}^* W_{2D}(\kappa_l, \varphi_l) \quad (20)$$

where $\kappa_l = \sqrt{\kappa_{lx}^2 + \kappa_{ly}^2}$ and $\varphi_l = \arctan(\kappa_{ly}/\kappa_{lx})$, with

$$\begin{aligned} \kappa_{lx} &= -k \sin \vartheta_{ls} \cos \varphi_{ls} + k \sin \vartheta_{li} \\ \kappa_{ly} &= -k \sin \vartheta_{ls} \sin \varphi_{ls} \end{aligned} \quad (21)$$

are modulus and direction of the facet local Bragg resonant wavenumber vector.

Finally,

$$\underline{\underline{\chi}}(\vartheta_{li}, \vartheta_{ls}, \varphi_{ls}, \beta_i, \beta_s) = \underline{\underline{R}}_2(\beta_s) \cdot \begin{pmatrix} F_{hh} & F_{hv} \\ F_{vh} & F_{vv} \end{pmatrix} \cdot \underline{\underline{R}}_2^{-1}(\beta_i) \quad (22)$$

where $\underline{\underline{R}}_2(\beta_{i,s})$ is the 2×2 rotation matrix [15], [28], accounting for the rotation of the local incidence and scattering planes with respect to the global ones, and $F_{pq}(\vartheta_{li}, \vartheta_{ls}, \varphi_{ls})$ are the bistatic Bragg coefficients [37], [38]

$$\begin{aligned} F_{hh} &= \frac{(\varepsilon - 1) \cos \varphi_{ls}}{[\cos \vartheta_{ls} + \sqrt{\varepsilon - \sin^2 \vartheta_{ls}}][\cos \vartheta_{li} + \sqrt{\varepsilon - \sin^2 \vartheta_{li}}]} \\ F_{vh} &= -\frac{\sin \varphi_{ls} (\varepsilon - 1) \sqrt{\varepsilon - \sin^2 \vartheta_{ls}}}{[\sqrt{\varepsilon - \sin^2 \vartheta_{ls}} + \varepsilon \cos \vartheta_{ls}][\cos \vartheta_{li} + \sqrt{\varepsilon - \sin^2 \vartheta_{li}}]} \\ F_{hv} &= \frac{\sin \varphi_{ls} (\varepsilon - 1) \sqrt{\varepsilon - \sin^2 \vartheta_{li}}}{[\sqrt{\varepsilon - \sin^2 \vartheta_{ls}} + \cos \vartheta_{ls}][\varepsilon \cos \vartheta_{li} + \sqrt{\varepsilon - \sin^2 \vartheta_{li}}]} \\ F_{vv} &= \frac{(\varepsilon - 1)[\sqrt{\varepsilon - \sin^2 \vartheta_{li}} \sqrt{\varepsilon - \sin^2 \vartheta_{ls}} \cos \varphi_{ls} - \varepsilon \sin \vartheta_{li} \sin \vartheta_{ls}]}{[\sqrt{\varepsilon - \sin^2 \vartheta_{ls}} + \varepsilon \cos \vartheta_{ls}][\varepsilon \cos \vartheta_{li} + \sqrt{\varepsilon - \sin^2 \vartheta_{li}}]} \end{aligned} \quad (23)$$

The local incidence ϑ_{li} and scattering ϑ_{ls} , φ_{ls} angles, and rotation angles β_i and β_s of the incidence and scattering planes, must be then expressed in terms of global incidence ϑ_i and scattering ϑ_s , φ_s angles and of local surface slopes s_x and s_y ; expressions for ϑ_{li} and β_i are already available in the literature [28], [39], and are reported here for the sake of completeness; conversely, the other ones are derived for the first time in this work, see Appendix A. All of them are listed in (24)–(28), as shown at the bottom of the next page.

It can be verified that in the backscattering direction, (24)–(28) lead to $\vartheta_{ls} = \vartheta_{li}$, $\beta_s = \beta_i$, and $\varphi_{ls} = \pi$.

C. Taylor Series Expansion and the Average Over Large-Scale Surface Slopes

Once (24)–(28) are inserted in (20)–(23), the bistatic covariance matrix elements of the tilted facet can be expanded in power series of facet slopes s_x and s_y ; by arresting the expansion to the second order, we get

$$\begin{aligned} R_{pq,rs}^{\text{SPM}}(\vartheta_i, \vartheta_s, \varphi_s; s_x, s_y) &\cong R_{pq,rs}^{\text{SPM}}(\vartheta_i, \vartheta_s, \varphi_s; 0, 0) \\ &+ D_{1,0}^{pq,rs} s_x + D_{0,1}^{pq,rs} s_y + D_{2,0}^{pq,rs} s_x^2 + D_{0,2}^{pq,rs} s_y^2 + D_{1,1}^{pq,rs} s_x s_y \end{aligned} \quad (29)$$

where

$$\begin{aligned} R_{pq,rs}^{\text{SPM}}(\vartheta_i, \vartheta_s, \varphi_s, 0, 0) &= \frac{4}{\pi} k^4 \cos^2 \vartheta_i \cos^2 \vartheta_s F_{pq}(\vartheta_i, \vartheta_s, \varphi_s) \\ &\times F_{rs}^*(\vartheta_i, \vartheta_s, \varphi_s) W_{2D}(\bar{\kappa}, \bar{\varphi}) \end{aligned} \quad (30)$$

is the usual SPM expression of the polarimetric covariance matrix

$$D_{k,n-k}^{pq,rs} = \frac{1}{n!} \binom{n}{k} \frac{\partial^n R_{pq,rs}^{\text{SPM}}}{\partial s_x^k \partial s_y^{n-k}} \Big|_{s_x=s_y=0} \quad (31)$$

and $\bar{\varphi} = \arctan(\bar{\kappa}_y/\bar{\kappa}_x)$ is the direction of the (global) Bragg resonant wavenumber vector, so that

$$\begin{aligned} \bar{\kappa}_y &= -k \sin \vartheta_s \sin \varphi_s \\ \bar{\kappa}_x &= -k \sin \vartheta_s \cos \varphi_s + k \sin \vartheta_i. \end{aligned} \quad (32)$$

Note that in (30) for $W_{2D}(\bar{\kappa}, \bar{\varphi})$, the exact PSD value at the Bragg wavenumber is used, whereas in order to compute the derivatives in (31), approximate expressions of (5)–(7) are used, to guarantee that analytical expressions can be always obtained.

Finally, the bistatic covariance matrix elements of the overall surface can be obtained by averaging (29) with respect to facet slopes, which is now straightforward:

$$\begin{aligned} \langle R_{pq,rs}^{\text{SPM}}(\vartheta_i, \vartheta_s, \varphi_s; s_x, s_y) \rangle_{s_x, s_y} &\cong R_{pq,rs}^{\text{SPM}}(\vartheta_i, \vartheta_s, \varphi_s; 0, 0) \\ &+ D_{2,0}^{pq,rs} \sigma_x^2 + D_{0,2}^{pq,rs} \sigma_y^2 + D_{1,1}^{pq,rs} \rho \sigma_x \sigma_y. \end{aligned} \quad (33)$$

Derivatives in (31) can be analytically computed in closed form by using (24)–(28) in (20)–(23) and applying the chain rule. Guidelines to their analytical evaluation are provided in Appendix B. Their expressions are rather involved, and in the general out-of-plane scattering case, although they allow the fast computation of bistatic scattering by anisotropic rough surfaces, they are not physically revealing. Therefore, we do not report here their full expressions for the out-of-plane scattering case: we believe that in this article, the interested reader can find all the elements to obtain closed form expressions of these derivatives, and hence of (33), by exploiting one of the several software tools currently commercially available for analytical calculus, see [42], [43]. Conversely, for scattering directions lying within the incidence plane, simpler closed-form expressions of (33) can be obtained, which can support the physical interpretation of the scattering process. They are reported in Section III-D.

D. In-Plane Scattering

As shown in Appendix B, for in-plane scattering, i.e., for $\varphi_s = n\pi$, with $n = 0, 1$, the bistatic covariance matrix elements of the overall surface in (33) can be expressed as

$$\begin{aligned} \langle \sigma_{hh}^{0SPM} \rangle &= C_{0,0}^{hh,hh} \Phi(0) \\ &\times \left[1 + \frac{C_{2,0}^{hh,hh}}{C_{0,0}^{hh,hh}} \sigma_x^2 + \left(\frac{C_{0,2}^{hh,hh}}{C_{0,0}^{hh,hh}} - (-1)^n \frac{2\text{Re}\{F_{vv}/F_{hh}\}}{\sin \vartheta_i \sin \vartheta_s} \right. \right. \\ &\quad \left. \left. - \frac{1}{\sin^2 \vartheta_i} - \frac{1}{\sin^2 \vartheta_s} + \frac{2\text{Re}\left\{ \frac{C_{0,1}^{hh,hv}}{\sin \vartheta_i} - (-1)^n \frac{C_{0,1}^{hh,vh}}{\sin \vartheta_s} \right\}}{C_{0,0}^{hh,hh}} \right) \sigma_y^2 \right] \end{aligned}$$

$$\begin{aligned} \langle \sigma_{vv}^{0SPM} \rangle &= C_{0,0}^{vv,vv} \Phi(0) \\ &\times \left[1 + \frac{C_{2,0}^{vv,vv}}{C_{0,0}^{vv,vv}} \sigma_x^2 + \left(\frac{C_{0,2}^{vv,vv}}{C_{0,0}^{vv,vv}} - (-1)^n \frac{2\text{Re}\{F_{hh}/F_{vv}\}}{\sin \vartheta_i \sin \vartheta_s} \right. \right. \\ &\quad \left. \left. - \frac{1}{\sin^2 \vartheta_i} - \frac{1}{\sin^2 \vartheta_s} + \frac{2\text{Re}\left\{ (-1)^n \frac{C_{0,1}^{vv,hv}}{\sin \vartheta_s} - \frac{C_{0,1}^{vv,vh}}{\sin \vartheta_i} \right\}}{C_{0,0}^{vv,vv}} \right) \sigma_y^2 \right] \end{aligned}$$

$$\begin{aligned} \langle \sigma_{hv}^{0SPM} \rangle &= C_{0,0}^{hh,hv} \Phi(0) \left(\frac{C_{0,2}^{hh,hv}}{C_{0,0}^{hh,hv}} + \frac{1}{F_{hh} F_{vv}^*} \left| \frac{F_{vv}}{\sin \vartheta_s} + (-1)^n \frac{F_{hh}}{\sin \vartheta_i} \right|^2 \right. \\ &\quad \left. - \frac{2\text{Re}\left\{ \frac{C_{0,1}^{hh,hv}}{\sin \vartheta_i} + (-1)^n \frac{C_{0,1}^{hh,vv}}{\sin \vartheta_s} \right\}}{C_{0,0}^{hh,hv}} \right) \sigma_y^2 \end{aligned}$$

$$\begin{aligned} \langle \sigma_{vh}^{0SPM} \rangle &= C_{0,0}^{hh,vh} \Phi(0) \left(\frac{C_{0,2}^{hh,vh}}{C_{0,0}^{hh,vh}} + \frac{1}{F_{hh} F_{vv}^*} \left| \frac{F_{vv}}{\sin \vartheta_i} + (-1)^n \frac{F_{hh}}{\sin \vartheta_s} \right|^2 \right. \\ &\quad \left. + \frac{2\text{Re}\left\{ \frac{C_{0,1}^{hh,vv}}{\sin \vartheta_i} + (-1)^n \frac{C_{0,1}^{hh,hv}}{\sin \vartheta_s} \right\}}{C_{0,0}^{hh,vh}} \right) \sigma_y^2 \end{aligned}$$

$$\begin{aligned} \langle R_{hh,vv}^{SPM} \rangle &= C_{0,0}^{hh,vv} \Phi(0) \\ &\times \left[1 + \frac{C_{2,0}^{hh,vv}}{C_{0,0}^{hh,vv}} \sigma_x^2 + \left(\frac{C_{0,2}^{hh,vv}}{C_{0,0}^{hh,vv}} - (-1)^n \frac{\frac{F_{hh}^*}{F_{vv}^*} + \frac{F_{vv}}{F_{hh}}}{\sin \vartheta_i \sin \vartheta_s} \right. \right. \\ &\quad \left. \left. - \frac{1}{\sin^2 \vartheta_i} - \frac{1}{\sin^2 \vartheta_s} + \frac{C_{0,1}^{hv,vv} - C_{0,1}^{hh,vh}}{C_{0,0}^{hh,vv} \sin \vartheta_i} \right. \right. \\ &\quad \left. \left. - (-1)^n \frac{C_{0,1}^{vh,vv} - C_{0,1}^{hh,hv}}{C_{0,0}^{hh,vv} \sin \vartheta_s} \right) \sigma_y^2 \right] \end{aligned}$$

$$\begin{aligned} \langle R_{hh,hv}^{SPM} \rangle &= C_{0,0}^{hh,hv} \Phi(0) \left[\frac{C_{1,1}^{hh,hv}}{C_{0,0}^{hh,hv}} + (-1)^n \frac{\cot \vartheta_s}{\sin \vartheta_s} - \frac{\cot \vartheta_i F_{hh}^*/F_{vv}^*}{\sin \vartheta_i} \right. \\ &\quad \left. - (-1)^n \frac{C_{1,0}^{hh,vv}}{C_{0,0}^{hh,vv} \sin \vartheta_s} - \frac{C_{1,0}^{hh,hh}}{C_{0,0}^{hh,hh} \sin \vartheta_i} \right] \rho \sigma_x \sigma_y \end{aligned}$$

$$\begin{aligned} \langle R_{hh,vh}^{SPM} \rangle &= C_{0,0}^{hh,vh} \Phi(0) \left[\frac{C_{1,1}^{hh,vh}}{C_{0,0}^{hh,vh}} + \frac{\cot \vartheta_i}{\sin \vartheta_i} - (-1)^n \frac{\cot \vartheta_s F_{hh}^*/F_{vv}^*}{\sin \vartheta_s} \right. \\ &\quad \left. + \frac{C_{1,0}^{hh,vv}}{C_{0,0}^{hh,vv} \sin \vartheta_i} + (-1)^n \frac{C_{1,0}^{hh,hh}}{C_{0,0}^{hh,hh} \sin \vartheta_s} \right] \rho \sigma_x \sigma_y \end{aligned}$$

$$\begin{aligned} \langle R_{hv,vv}^{SPM} \rangle &= C_{0,0}^{hh,vv} \Phi(0) \left[\frac{C_{1,1}^{hv,vv}}{C_{0,0}^{hh,vv}} - \frac{\cot \vartheta_i}{\sin \vartheta_i} + (-1)^n \frac{\cot \vartheta_s F_{vv}/F_{hh}}{\sin \vartheta_s} \right. \\ &\quad \left. - \frac{C_{1,0}^{hh,vv}}{C_{0,0}^{hh,vv} \sin \vartheta_i} - (-1)^n \frac{C_{1,0}^{vv,vv}}{C_{0,0}^{hh,vv} \sin \vartheta_s} \right] \rho \sigma_x \sigma_y \end{aligned}$$

$$\begin{aligned} \langle R_{vh,vv}^{SPM} \rangle &= C_{0,0}^{hh,vv} \Phi(0) \left[\frac{C_{1,1}^{vh,vv}}{C_{0,0}^{hh,vv}} - (-1)^n \frac{\cot \vartheta_s}{\sin \vartheta_s} + \frac{\cot \vartheta_i F_{vv}/F_{hh}}{\sin \vartheta_i} \right. \\ &\quad \left. + (-1)^n \frac{C_{1,0}^{hh,vv}}{C_{0,0}^{hh,vv} \sin \vartheta_s} + \frac{C_{1,0}^{vv,vv}}{C_{0,0}^{hh,vv} \sin \vartheta_i} \right] \rho \sigma_x \sigma_y \end{aligned}$$

$$\cos \vartheta_{li} = \frac{\cos \vartheta_i + s_x \sin \vartheta_i}{\sqrt{1 + s_x^2 + s_y^2}} \quad (24)$$

$$\tan \beta_i = \frac{s_y}{\sin \vartheta_i - s_x \cos \vartheta_i} \quad (25)$$

$$\cos \vartheta_{ls} = \frac{\cos \vartheta_s - s_x \sin \vartheta_s \cos \varphi_s - s_y \sin \vartheta_s \sin \varphi_s}{\sqrt{1 + s_x^2 + s_y^2}} \quad (26)$$

$$\begin{aligned} \cos \varphi_{ls} &= \frac{1}{\sqrt{(\sin \vartheta_i - s_x \cos \vartheta_i)^2 + s_y^2}} \\ &\times \left(\frac{(\sin \vartheta_i - s_x \cos \vartheta_i)(\sin \vartheta_s \cos \varphi_s + s_x \cos \vartheta_s)}{\sqrt{(\sin \vartheta_s \cos \varphi_s + s_x \cos \vartheta_s)^2 + (-s_y \cos \vartheta_s - \sin \vartheta_s \sin \varphi_s)^2 + (-s_x \sin \vartheta_s \sin \varphi_s + s_y \sin \vartheta_s \cos \varphi_s)^2}} \right. \\ &\quad \left. + \frac{s_y \cos \vartheta_i (-s_y \cos \vartheta_s - \sin \vartheta_s \sin \varphi_s) + s_y \sin \vartheta_i (-s_x \sin \vartheta_s \sin \varphi_s + s_y \sin \vartheta_s \cos \varphi_s)}{\sqrt{(\sin \vartheta_s \cos \varphi_s + s_x \cos \vartheta_s)^2 + (-s_y \cos \vartheta_s - \sin \vartheta_s \sin \varphi_s)^2 + (-s_x \sin \vartheta_s \sin \varphi_s + s_y \sin \vartheta_s \cos \varphi_s)^2}} \right) \quad (27) \end{aligned}$$

$$\tan \beta_s = \frac{s_x \sin \varphi_s - s_y \cos \varphi_s}{\sin \vartheta_s + s_x \cos \vartheta_s \cos \varphi_s + s_y \cos \vartheta_s \sin \varphi_s} \quad (28)$$

$$\begin{aligned}
\langle R_{hv,vh}^{\text{SPM}} \rangle &= C_{0,0}^{hh,vv} \Phi(0) \\
&\times \left[\frac{C_{0,2}^{hv,hv}}{C_{0,0}^{hh,vv}} - \frac{1}{F_{hh} F_{vv}^*} \left(\frac{F_{vv} F_{hh}^*}{\sin^2 \vartheta_s} + \frac{F_{hh} F_{vv}^*}{\sin^2 \vartheta_i} \right. \right. \\
&\quad \left. \left. + (-1)^n \frac{|F_{hh}|^2 + |F_{vv}|^2}{\sin \vartheta_i \sin \vartheta_s} \right) + \frac{C_{0,1}^{hv,vv} - C_{0,1}^{hh,vh}}{C_{0,0}^{hh,vv} \sin \vartheta_i} \right. \\
&\quad \left. - (-1)^n \frac{C_{0,1}^{vh,vv^*} - C_{0,1}^{hh,hv^*}}{C_{0,0}^{hh,vv} \sin \vartheta_s} \right] \sigma_y^2 \quad (34)
\end{aligned}$$

where

$$C_{k,n-k}^{pq,rs} = \frac{4}{\pi} k^4 \frac{1}{n!} \binom{n}{k} \frac{\partial^n \cos^2 \vartheta_i \cos^2 \vartheta_s F_{pq} F_{rs}^* W(\kappa_l)}{\partial s_x^k \partial s_y^{n-k}} \Big|_{s_x=s_y=0} \quad (35)$$

and

$$\Phi(0) = 1 + \Delta \cos(2\varphi_0). \quad (36)$$

Note that

$$\begin{aligned}
C_{0,0}^{pq,rs} &= \frac{4}{\pi} k^4 \cos^2 \vartheta_i \cos^2 \vartheta_s F_{pq}(\vartheta_i, \vartheta_s, \varphi_s) \\
&\quad \times F_{rs}^*(\vartheta_i, \vartheta_s, \varphi_s) W(\bar{\kappa}) \quad (37)
\end{aligned}$$

is the usual SPM expression of the polarimetric covariance matrix of an isotropic rough surface.

It can be verified (see also Appendix B) that in the backscattering direction, identified by $\vartheta_s = \vartheta_i$ and $\varphi_s = \pi$, cross-polarized NRCSs coincide ($\langle \sigma_{hv}^{\text{SPM}} \rangle = \langle \sigma_{vh}^{\text{SPM}} \rangle = \langle R_{hv,vh}^{\text{SPM}} \rangle$) and (34)–(36) lead to the A-PTSM expressions reported in [28].

It must be recalled that the SPM, and hence (33) and (34), is not accurate around the specular direction (for which $\bar{\kappa} = 0$), i.e., for small values of $\bar{\kappa}$. Therefore, we can safely use (33) and (34) only for $\bar{\kappa} > \kappa_{\text{cut}}$. When we use (33) or (34) in conjunction with (13) in (12) to compute the co-polarized NRCSs and correlations, we will multiply them by $\tanh[(\bar{\kappa}/\kappa_{\text{cut}})^6]$, which very closely approximates one for $\bar{\kappa} > \kappa_{\text{cut}}$ and rapidly goes 0 for $\bar{\kappa} < \kappa_{\text{cut}}$. We heuristically choose $\kappa_{\text{cut}} = 3k(\sigma_x \sigma_y)^{1/2}$, which in most cases ensures a smooth transition from the SPM to GO at scattering directions approaching the specular one. This choice slightly affects the scattering results only for scattering directions in the very narrow angular region where GO and SPM contributions are of the same order. Therefore, in most cases, the results of our method are independent of the choice of the cutoff wavenumber. It must be noted that our heuristic choice also has a physical justification: as the rms slopes increase, the cutoff wavenumber must increase to keep a low probability that, while using the SPM, a tilted facet is at such an angle that renders the scattering direction coincident with the specular one.

Equation (34) shows that, for the in-plane scattering case, all the correlations between a co-polar and a cross-polar channel vanish if $\rho = 0$, that is, see (9), if the large-scale roughness is isotropic, i.e., $\sigma_x^2 = \sigma_y^2$, or if ψ is 0 or an integer multiple of $\pi/2$. For a sea surface, this happens if the transmitter viewing direction is exactly upwind, crosswind, or downwind; for a

tilled soil, if the transmitter viewing direction is perpendicular or parallel to the plowing direction.

It is also interesting to note that according to (34), the cross-polar NRCSs and correlation are directly proportional to the variance of slopes along the y direction. This has useful implications both for tilled soils and for sea surfaces. In fact, in the former case, for which $\Phi(0) \equiv 1$, this implies that cross-polar NRCSs and correlation are more sensitive to the plowing direction than the other elements of the polarimetric covariance matrix, due to the $\cos 2\psi$ dependence of σ_y^2 . This is in agreement with the numerical results obtained in [44] for the backscattering case. Conversely, for sea surfaces, $\Phi(0)$ and σ_y^2 produce oscillations of the kind $\cos 2\varphi_w$ of opposite sign, see (8) and (36), so that they tend to cancel out, and hence, the dependence of cross-polar NRCSs and correlation on wind direction is weakened with respect to the one of the other elements of the polarimetric covariance matrix. This is in agreement with experimental data obtained in the backscattering case [45]. In addition, dependence on wind speed intensity appears both in $C_{0,0}^{hh,vv}$ and in σ_y^2 , so that dependence of cross-polar NRCSs and correlation on wind velocity is stronger than the one of the other elements of the polarimetric covariance matrix. This is in agreement with experimental data obtained in the backscattering case [45], too. However, it is important to note that these implications do not hold for nearly specular directions, where the scattering behavior is dictated by the GO contribution. In particular, GO terms depend on wind only through the exponential factor in (13): indeed, using (10), it is easy to see that the remaining GO factor is independent on the angle ψ . This implies that NRCS evaluated exactly in the specular direction present no dependence on wind direction, since in this configuration, as already mentioned in Section III-A, the argument of the exponential in (13) vanishes.

A few last words are needed on validity limits of the method. With regard to sea conditions, the same limitations as in the monostatic case [28] apply: we can expect that the presented approach can be safely used for wind speeds not smaller than 4 m/s and smaller than about 20 m/s, which ensures that the effect of breaking waves on scattering can be neglected and that σ_x and σ_y are smaller than about 0.2. This last condition must hold also for tilled soil surfaces. By the way, it also ensures that our cutoff wavenumber is of the order of, or smaller than, $k/2$.

Finally, our approach cannot be used at small grazing angles, since shadowing is neglected. Conversely, the presented method can be used at all frequencies of interest for microwave remote sensing.

E. Circular Basis

Expressions similar to (13) and (33) can be obtained in circular polarization basis. In fact, for GO, we can write

$$\begin{aligned}
\tilde{R}_{PQ,RS}^{\text{GO}} &= \frac{\tilde{S}_{PQ} \tilde{S}_{RS}^*}{2\sigma_x \sigma_y \sqrt{1 - \rho^2} (\cos \vartheta_i + \cos \vartheta_s)^4} \\
&\quad \exp \left\{ - \frac{\sigma_x^2 \bar{\kappa}_y^2 + \sigma_y^2 \bar{\kappa}_x^2 - 2\sigma_x \sigma_y \rho \bar{\kappa}_x \bar{\kappa}_y}{2k^2 \sigma_x^2 \sigma_y^2 (1 - \rho^2) (\cos \vartheta_i + \cos \vartheta_s)^2} \right\} \quad (38)
\end{aligned}$$

where P , Q , R , and S may each stand for R (right-handed polarization) or L (left-handed polarization), and

$$\underline{\tilde{S}} = \underline{U}_{l \rightarrow c}^* \cdot \underline{S} \cdot \underline{U}_{l \rightarrow c}^{-1} \quad (39)$$

with $\underline{U}_{l \rightarrow c}$ being the matrix of the linear to circular polarization basis change [15]

$$\underline{U}_{l \rightarrow c} = \frac{1}{\sqrt{2}} \begin{pmatrix} 1 & -j \\ -j & 1 \end{pmatrix}. \quad (40)$$

Equation (38) is particularly simple for the diagonal elements of the polarimetric covariance matrix, i.e., for the NRCSs

$$\begin{aligned} \tilde{\sigma}_{RL}^{\text{GO}} = \tilde{\sigma}_{LR}^{\text{GO}} &= \frac{(2 \cos \vartheta_0)^4 \left| \frac{\Gamma_h(\vartheta_0) + \Gamma_h(\vartheta_0)}{2} \right|^2}{2\sigma_x \sigma_y \sqrt{1 - \rho^2} (\cos \vartheta_i + \cos \vartheta_s)^4} \\ &\times \exp \left\{ - \frac{\sigma_x^2 \bar{\kappa}_y^2 + \sigma_y^2 \bar{\kappa}_x^2 - 2\sigma_x \sigma_y \rho \bar{\kappa}_x \bar{\kappa}_y}{2k^2 \sigma_x^2 \sigma_y^2 (1 - \rho^2) (\cos \vartheta_i + \cos \vartheta_s)^2} \right\} \end{aligned} \quad (41)$$

$$\begin{aligned} \tilde{\sigma}_{RR}^{\text{GO}} = \tilde{\sigma}_{LL}^{\text{GO}} &= \frac{(2 \cos \vartheta_0)^4 \left| \frac{\Gamma_h(\vartheta_0) - \Gamma_h(\vartheta_0)}{2} \right|^2}{2\sigma_x \sigma_y \sqrt{1 - \rho^2} (\cos \vartheta_i + \cos \vartheta_s)^4} \\ &\times \exp \left\{ - \frac{\sigma_x^2 \bar{\kappa}_y^2 + \sigma_y^2 \bar{\kappa}_x^2 - 2\sigma_x \sigma_y \rho \bar{\kappa}_x \bar{\kappa}_y}{2k^2 \sigma_x^2 \sigma_y^2 (1 - \rho^2) (\cos \vartheta_i + \cos \vartheta_s)^2} \right\}. \end{aligned} \quad (42)$$

The SPM expression for the covariance matrix of a tilted facet in circular polarization basis is

$$\tilde{R}_{PQ,RS}^{\text{SPM}} = \frac{4}{\pi} k^4 \cos^2 \vartheta_{li} \cos^2 \vartheta_{ls} \tilde{\chi}_{PQ} \tilde{\chi}_{RS}^* W_{2D}(\kappa_l, \varphi_l) \quad (43)$$

where

$$\tilde{\chi} = \underline{U}_{l \rightarrow c}^* \cdot \underline{\chi} \cdot \underline{U}_{l \rightarrow c}^{-1}. \quad (44)$$

By proceeding as in the linear polarization basis case, i.e., by expanding in power series of facet slopes s_x and s_y and averaging with respect to facet slopes, we get

$$\begin{aligned} \langle \tilde{R}_{PQ,RS}^{\text{SPM}}(\vartheta_i, \vartheta_s, \varphi_s; s_x, s_y) \rangle_{s_x, s_y} \\ \cong \tilde{R}_{PQ,RS}^{\text{SPM}}(\vartheta_i, \vartheta_s, \varphi_s; 0, 0) \\ + \tilde{D}_{2,0}^{PQ,RS} \sigma_x^2 + \tilde{D}_{0,2}^{PQ,RS} \sigma_y^2 + \tilde{D}_{1,1}^{PQ,RS} \rho \sigma_x \sigma_y \end{aligned} \quad (45)$$

where

$$\tilde{D}_{k,n-k}^{PQ,RS} = \frac{1}{n!} \binom{n}{k} \left. \frac{\partial^n \tilde{R}_{PQ,RS}^{\text{SPM}}}{\partial s_x^k \partial s_y^{n-k}} \right|_{s_x=s_y=0}. \quad (46)$$

Derivatives in (46) can be analytically computed in closed form by using (24)–(28) in (43) and (44) and applying the chain rule, along the same guidelines provided for the case of linear polarization basis. Their expressions are rather involved, and we do not report here their full expressions: again, we believe that in this article the interested reader can find all the elements to obtain closed form expressions of these derivatives, and hence of (33), by exploiting one of the several software tools currently commercially available for analytical calculus [42], [43].

IV. NUMERICAL RESULTS

In this section, we report the numerical results regarding two meaningful cases of anisotropic surfaces, i.e., wind-driven sea surfaces and agricultural tilled surfaces.

A. Wind-Driven Sea Surface

We consider the wind-driven sea surface model detailed in Section II-B. For this case, the presented numerical results illustrate the polarimetric bistatic scattering dependence on scattering angles and wind direction, fixing a 45° incidence angle, L-band (frequency = 1.58 GHz and $\varepsilon = 65 - j61$), and for a fresh breeze (wind speed = 10 m/s). This specific configuration is the same considered in [26] for the presentation of SSA2, thus facilitating the comparison between our BA-PTSM and SSA2.

In Fig. 2, we show the diagonal elements of the covariance matrix, i.e., NRCSs, as a function of the zenith scattering angle ϑ_s , for up-wind ($\phi_w = 0$) configuration and for several azimuth scattering angles. For cases (a)–(d), the results obtained with our model are directly compared with those obtained in [26] by using SSA2, reported as dots. The graphs confirm the good agreement of the BA-PTSM with the SSA2 results, with difference of few decibels over a whole range of zenith scattering angles for most cases. For cross-polarized in-plane scattering GO contributions are 0 [see (14) or (19) for $\phi_s = 0$] and since the SPM does not hold for close-to-specular directions, the cross-pol graphs have not been plotted in this region in Fig. 2(a). However, it is worth to underline that the cross-polarized contributions should be 0 also according to the nontilted SPM, so that the graphs of Fig. 2(a) can be evaluated only thanks to the second-order terms considered in our scattering formulation [see (37) for $\phi_s = 0^\circ$]. In Fig. 2(c), the vv NRCS exhibits a minimum located in the same position of the one predicted by SSA2: this is related to the minimum of the vv Bragg coefficient of (23), which leads to the same condition mentioned in [26]. The difference in the depth of this minimum may be partly due to the discretization used in [26] for SSA2 numerical evaluation. Finally, from Fig. 2(d), it can be appreciated that the hh NRCS is underestimated of up to 4 dB with respect to SSA2. It is worth noting that in this case the first-order hh SPM term is 0 [see (37) for $\phi_s = 90^\circ$], so that the graph in Fig. 2(d) is related to GO and second-order terms of our development. Moreover, it must be underlined that, differently from SSA2, which requires evaluation of fourfold integrals with highly oscillating integrands, our formulation is completely in closed form (including expressions of the sea-surface slope variances) and the whole set of plots of Fig. 2 is obtained in a time of the order of minutes with a common laptop.

In Fig. 3, the modulus of the off-diagonal correlation terms of the polarimetric covariance matrix is shown. In particular, in Fig. 3(a), the hh, vv and hv, vh correlations are the only nonzero contributions: more specifically, it is worth noting that the latter would be null according to both the SPM without random tilt and GO. Therefore, similar to Fig. 2(a), in this case, the BA-PTSM does not hold for close-to-specular directions and the graph has not been plotted. Moreover,

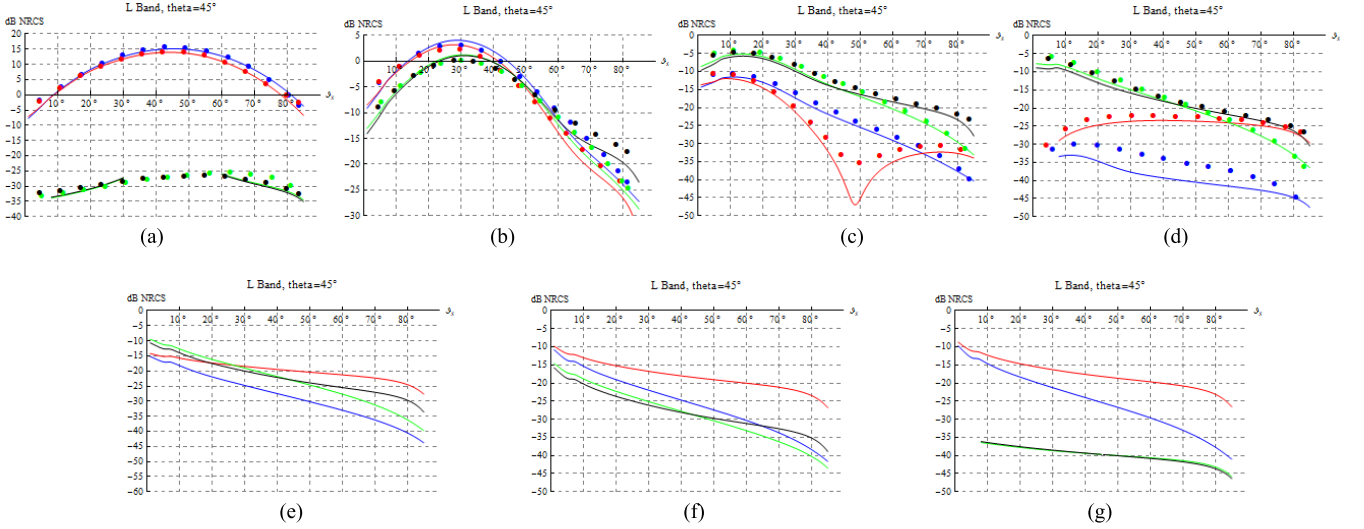


Fig. 2. NRCS (hh in blue, vv in red, hv in green, and vh in black) as a function of the zenith scattering angle ϑ_s at L-band (frequency = 1.58 GHz and $\varepsilon = 65 - j61$) for the sea surface in the presence of a fresh breeze (wind speed = 10 m/s), up-wind ($\phi_w = 0$), and azimuth scattering angles: (a) $\phi_s = 0^\circ$; (b) $\phi_s = 30^\circ$; (c) $\phi_s = 60^\circ$; (d) $\phi_s = 90^\circ$; (e) $\phi_s = 120^\circ$; (f) $\phi_s = 150^\circ$; (g) $\phi_s = 180^\circ$. For cases (a)–(d), the results obtained with the SSA2 model are reported as dots (hh in blue, vv in red, hv in green, and vh in black).

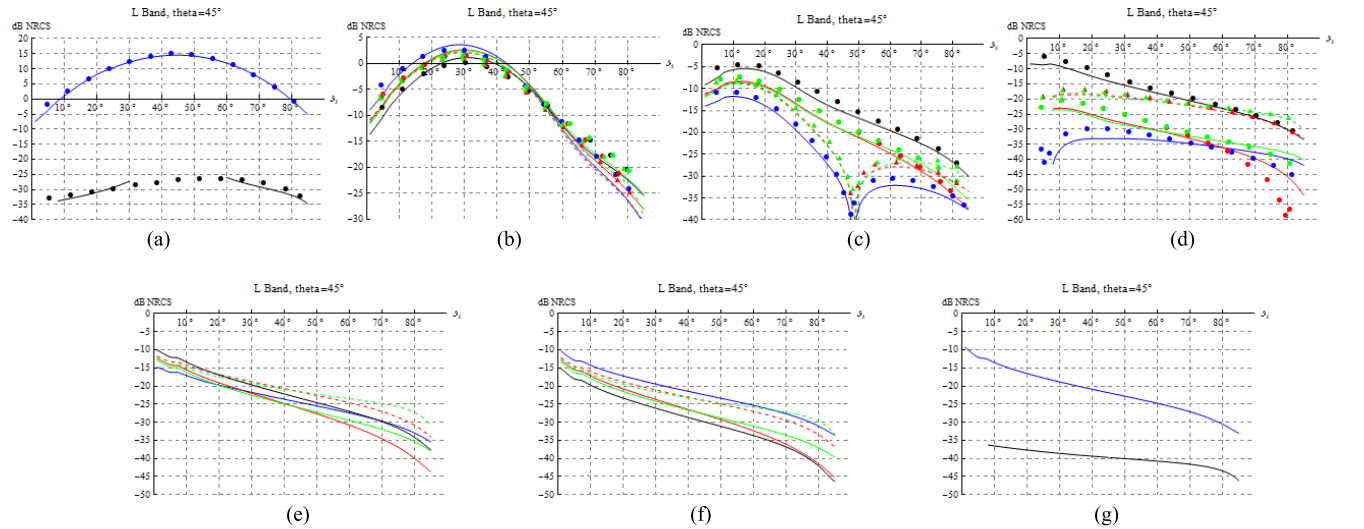


Fig. 3. Off-diagonal terms (modulus) of the polarimetric covariance matrix ($hhvv$ in blue, $hhhv$ in red, $hhvh$ in green, $hvvv$ in dashed red, $hvvh$ in dashed green, and $hvhv$ in black) as a function of the zenith scattering angle ϑ_s at L-band (frequency = 1.58 GHz and $\varepsilon = 65 - j61$) for the sea surface in the presence of a fresh breeze (wind speed = 10 m/s), up-wind ($\phi_w = 0$), and azimuth scattering angles: (a) $\phi_s = 0^\circ$; (b) $\phi_s = 30^\circ$; (c) $\phi_s = 60^\circ$; (d) $\phi_s = 90^\circ$; (e) $\phi_s = 120^\circ$; (f) $\phi_s = 150^\circ$; (g) $\phi_s = 180^\circ$. For cases (a)–(d), the results obtained with the SSA2 model are reported as dots ($hhvv$ in blue, $hhhv$ in red, $hhvh$ in green, and $hvvv$ in black) and triangles ($hvvv$ in red and $hvvh$ in green).

it is worth noting that, similar to Fig. 2(d), the $hh, vv, hh, hv,$ and hh, vh elements would be null according to the SPM without random tilt. In cases (a)–(d), a good agreement with the SSA2 results is obtained also for the off-diagonal elements.

In Fig. 4, we show the RR and RL NRCS in the same cases of Figs. 2 and 3. Also in this case, the obtained results are in very good agreement with SSA2 ones, reported as dots in Fig. 4. In particular, our graphs are closer to SSA2 ones than to those of the first-order small-slope approximation SSA1, reported as triangles in Fig. 4.

Analysis of scattering dependence on wind direction is now in order: the case of in-plane scattering with $\phi_s = 0^\circ$ is here considered. In Fig. 5, the diagonal elements of the polarimetric

covariance matrix are considered, both for the linear and the circular polarization. For Fig. 5(a)–(d), the results are compared with those relevant to SSA2: a good agreement is obtained. In particular, from Fig. 5(c), it is evident that the graphs of the BA-PTSM are closer to the ones of SSA2 than to those of SSA1. Finally, it is worth noting that the theoretical predictions of Section III-D are confirmed by Fig. 5(b), where the very weak dependence of the cross-polarized NRCS on wind direction can be appreciated.

B. Tilled Agricultural Soil

We consider the tilled agricultural soil surface model outlined in Section II-C. In this case, the presented numerical

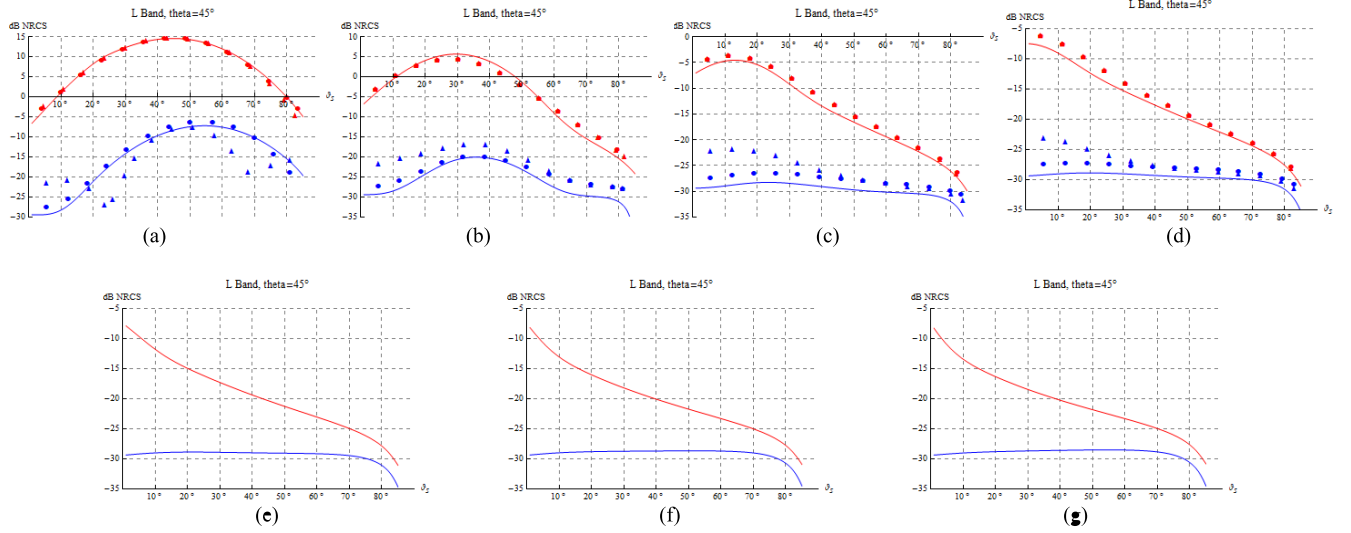


Fig. 4. Circular polarization NRCS terms of the polarimetric covariance matrix (RR in blue and RL in red) as a function of the zenith scattering angle ϑ_s at L-band (frequency = 1.58 GHz and $\varepsilon = 65 - j61$) for the sea surface in the presence of a fresh breeze (wind speed = 10 m/s), up-wind ($\phi_w = 0$), and azimuth scattering angles: (a) $\phi_s = 0^\circ$; (b) $\phi_s = 30^\circ$; (c) $\phi_s = 60^\circ$; (d) $\phi_s = 90^\circ$; (e) $\phi_s = 120^\circ$; (f) $\phi_s = 150^\circ$; (g) $\phi_s = 180^\circ$. For cases (a)–(d), the results obtained with the SSA1 and SSA2 models are reported as triangles and dots (RR in blue and RL in red), respectively.

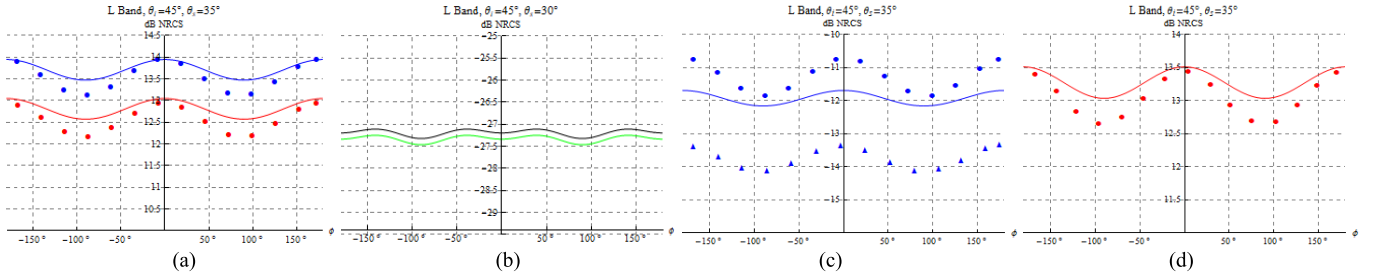


Fig. 5. NRCS behavior as a function of wind direction ϕ_w at L-band (frequency = 1.58 GHz and $\varepsilon = 65 - j61$) for the sea surface in the presence of a fresh breeze (wind speed = 10 m/s) and $\phi_s = 0^\circ$. (a) Linear polarization co-polarized NRCS, $\vartheta_s = 35^\circ$ (hh in blue and vv in red). (b) Linear polarization cross-polarized NRCS, $\vartheta_s = 30^\circ$ (hv in green and vh in black). (c) Circular polarization RR , $\vartheta_s = 35^\circ$. (d) Circular polarization RL , $\vartheta_s = 35^\circ$. For cases (a)–(d), the results obtained with the SSA2 model are reported as dots. For case (c), the results obtained with the SSA1 model are reported as triangles.

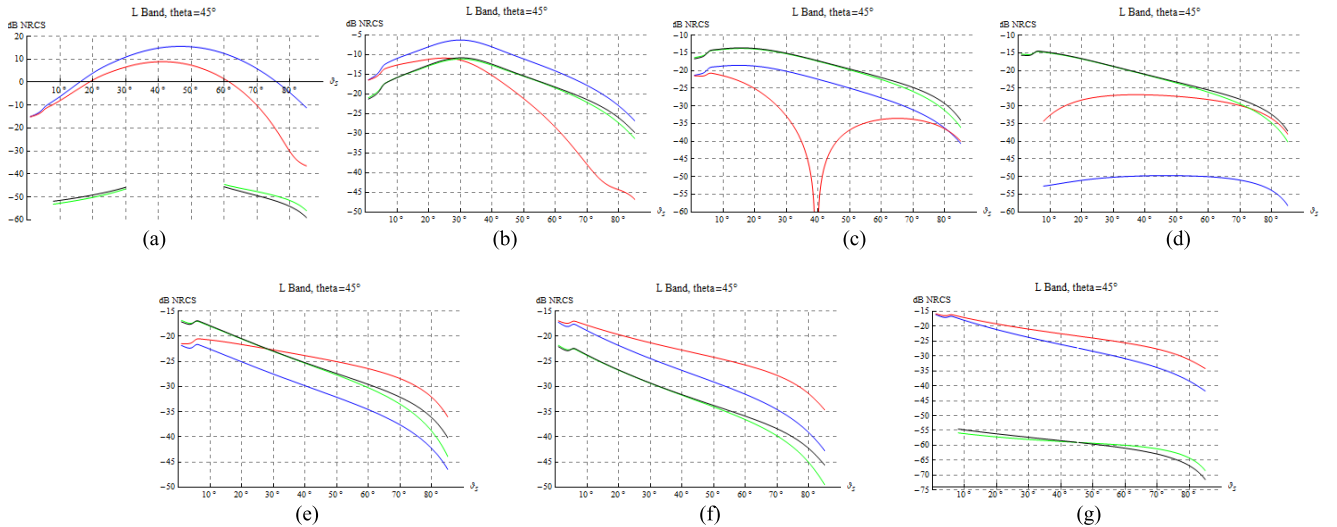


Fig. 6. NRCS (hh in blue, vv in red, hv in green, and vh in black) as a function of the zenith scattering angle ϑ_s at L-band (frequency = 1.58 GHz and $\varepsilon = 4$) for a tilled agricultural soil with $\psi = 0$ and azimuth scattering angles: (a) $\phi_s = 0^\circ$; (b) $\phi_s = 30^\circ$; (c) $\phi_s = 60^\circ$; (d) $\phi_s = 90^\circ$; (e) $\phi_s = 120^\circ$; (f) $\phi_s = 150^\circ$; (g) $\phi_s = 180^\circ$.

results illustrate the polarimetric bistatic scattering dependence on scattering angles and tillage direction, fixing a 45° incidence angle, L-band (frequency = 1.58 GHz) and relative permittivity $\varepsilon = 4$ (roughly corresponding to a dry soil). As for

the isotropic small-scale roughness, we considered typical fractal parameters of soil (see [46], [47] for a discussion), setting $H = 0.7$ and $S_0 = 0.01 \text{ m}^{0.6}$. Regarding the large-scale roughness, we fixed $\sigma_Y = 0.03$ and $\sigma_X = \sqrt{10}\sigma_Y$.

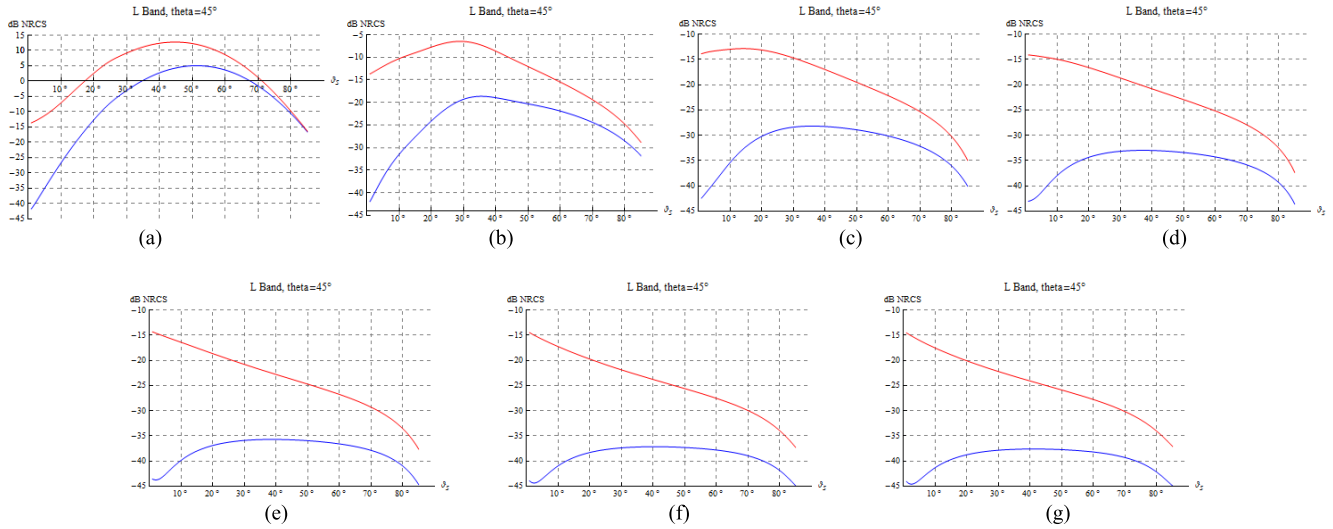


Fig. 7. Circular polarization NRCS terms of the polarimetric covariance matrix (RR in blue and RL in red) as a function of the zenith scattering angle ϑ_s at L-band (frequency = 1.58 GHz and $\epsilon = 4$) for a tilled agricultural soil with $\psi = 0$ and azimuth scattering angles: (a) $\phi_s = 0^\circ$; (b) $\phi_s = 30^\circ$; (c) $\phi_s = 60^\circ$; (d) $\phi_s = 90^\circ$; (e) $\phi_s = 120^\circ$; (f) $\phi_s = 150^\circ$; (g) $\phi_s = 180^\circ$.

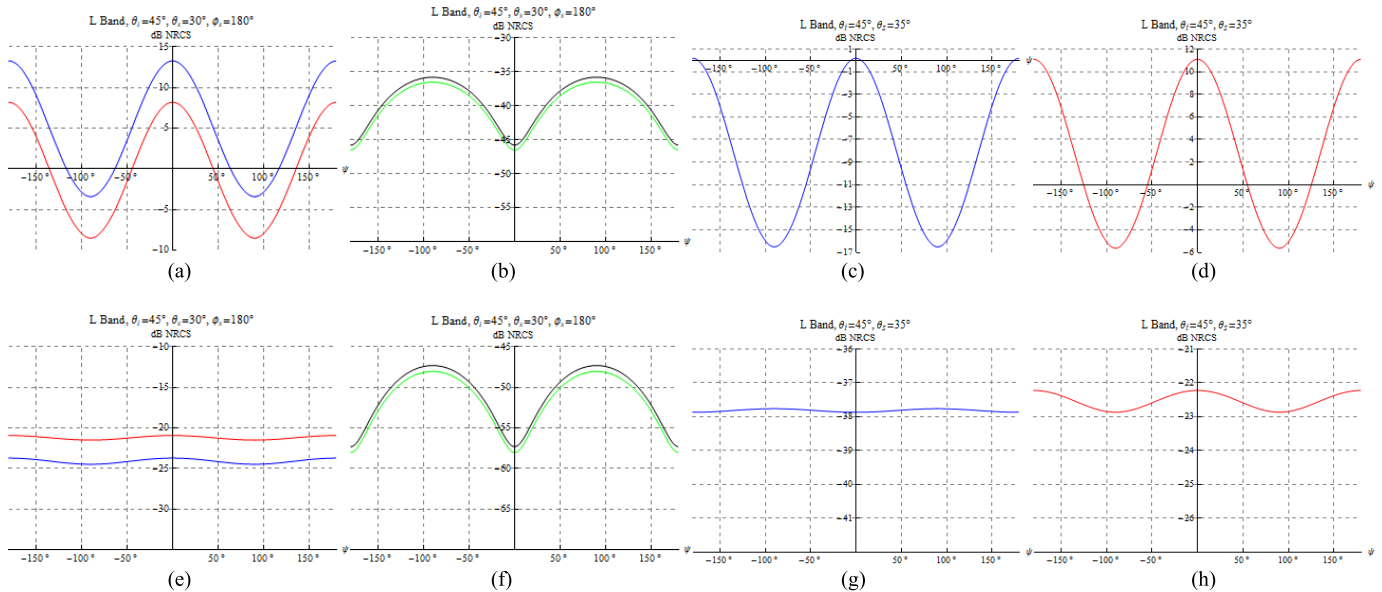


Fig. 8. NRCS as a function of the plowing direction ψ at L-band (frequency = 1.58 GHz and $\epsilon = 4$) for a tilled agricultural soil. (a) Linear polarization co-polarized NRCS, $\phi_s = 0^\circ$ and $\vartheta_s = 35^\circ$ (hh in blue and vv in red). (b) Linear polarization cross-polarized NRCS, $\phi_s = 0^\circ$ and $\vartheta_s = 30^\circ$ (hv in green and vh in black). (c) Circular polarization RR , $\phi_s = 0^\circ$ and $\vartheta_s = 35^\circ$. (d) Circular polarization RL , $\phi_s = 0^\circ$ and $\vartheta_s = 35^\circ$. (e) Linear polarization co-polarized NRCS, $\phi_s = 180^\circ$ and $\vartheta_s = 30^\circ$ (hh in blue and vv in red). (f) Linear polarization cross-polarized NRCS, $\phi_s = 180^\circ$ and $\vartheta_s = 30^\circ$ (hv in green and vh in black). (g) Circular polarization RR , $\phi_s = 180^\circ$ and $\vartheta_s = 30^\circ$. (h) Circular polarization RL , $\phi_s = 180^\circ$ and $\vartheta_s = 30^\circ$.

In Fig. 6, we show diagonal NRCS elements of the covariance matrix as a function of the zenith scattering angle ϑ_s , for plowing direction along the y -axis, i.e., $\psi = 0$, and for the same set of azimuth scattering angles considered in Fig. 2. Due to the low σ_y , low values of the cross-polarized NRCS, which unlike the co-polarized ones depend on σ_y only [see (34)], are obtained in Fig. 6(a) and (g). It is also worth noting that the same minimum of the vv NRCS observed in Fig. 2(c) is present in Fig. 6(c): in this case, however, the depth of the minimum is more pronounced and this is due to the fact that the dielectric permittivity is now real valued, so that the vv Bragg coefficient of (23) can be exactly equal to 0. In Fig. 7,

also the graphs of the RR and RL NRCS are shown for the same scattering configuration of Fig. 6.

The analysis of the behavior of the NRCS as a function of plowing direction is particularly interesting in this situation, due to the presence of strong anisotropy. Indeed, in Fig. 8, some meaningful examples are considered: both cases of in-plane scattering with $\phi_s = 0^\circ$ and $\phi_s = 180^\circ$ are analyzed. Regarding $\phi_s = 0^\circ$, in Fig. 8(a)–(d), the same scattering configurations of Fig. 5 are considered. Wide oscillations of about 15 and 10 dB are experienced by the co-polarized and cross-polarized NRCS coefficients in Fig. 8(a) and (b), respectively. Oscillations reach a value of almost 17 dB for

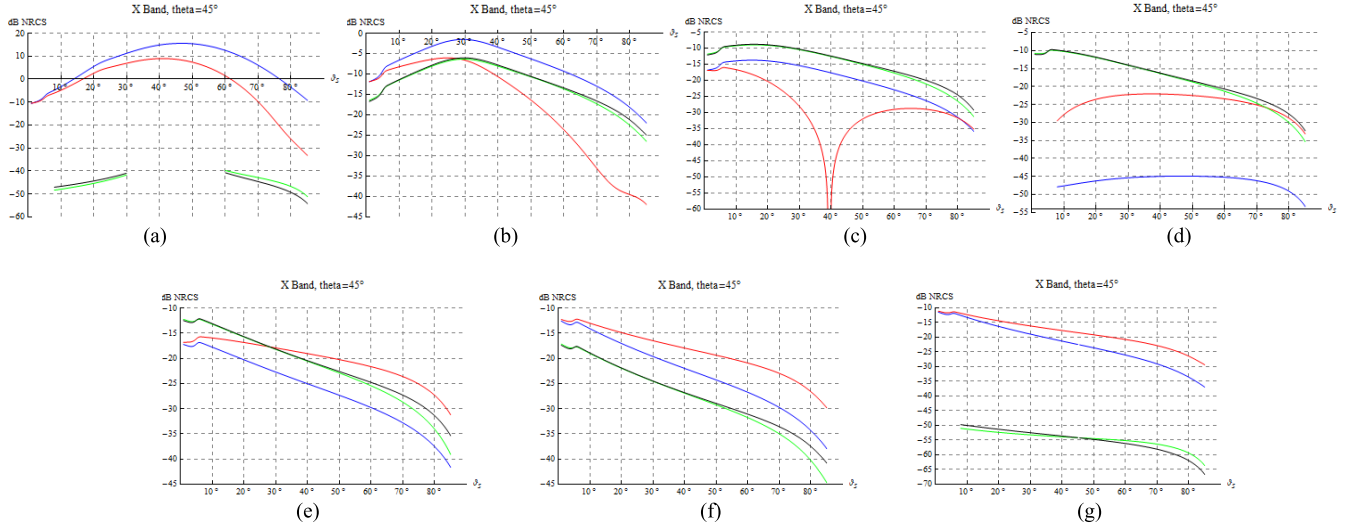


Fig. 9. NRCS (hh in blue, vv in red, hv in green, and vh in black) as a function of the zenith scattering angle ϑ_s at X-band (frequency = 10 GHz and $\varepsilon = 4$) for a tilled agricultural soil with $\psi = 0$ and azimuth scattering angles: (a) $\phi_s = 0^\circ$; (b) $\phi_s = 30^\circ$; (c) $\phi_s = 60^\circ$; (d) $\phi_s = 90^\circ$; (e) $\phi_s = 120^\circ$; (f) $\phi_s = 150^\circ$; (g) $\phi_s = 180^\circ$.

the circular polarizations RR and RL NRCS of Fig. 8(c) and (d). Finally, Fig. 8(e)–(h) illustrates the case of in-plane scattering with $\phi_s = 180^\circ$: in this region, far from the specular direction, we can better assess the implications reported in Section III-D. In particular, we can observe how the oscillations of the cross-polarized NRCS in Fig. 8(f) are much larger than those of the co-polarized NRCS in Fig. 8(e), as expected for the case of tilled agricultural soil. Finally, a weak dependence on plowing direction is observed in this configuration for the circular polarizations NRCS shown in Fig. 8(g) and (h).

We explicitly note that Fig. 8 clearly illustrates the importance of considering surface anisotropy: had we ignored it, all graphs of Fig. 8 would have been perfectly flat.

Finally, we show the results obtained at X-band (frequency = 10 GHz), again with a 45° incidence angle and relative permittivity $\varepsilon = 4$. In particular, in Fig. 9, we report the NRCS elements of the covariance matrix as a function of the zenith scattering angle ϑ_s , for plowing direction along the y -axis, i.e., $\psi = 0$, and for the same set of azimuth scattering angles considered at the L-band in Fig. 6. Comments analogous to those made for the L-band can be made in this case.

V. CONCLUSION

We have extended the A-PTSM to deal with the case of bistatic electromagnetic scattering, and we have applied it to scattering from wind-driven sea surfaces and from tilled agricultural fields. In doing this, we have derived for the first time the relationship between local scattering angles and scattering plane rotation angle on one side, and global scattering angles and surface slopes on the other side.

All the elements of the polarimetric covariance matrix have been analytically expressed in closed form, both in the linear and in the circular polarization bases, so that no numerical integration is needed by our method. This

renders all computations very fast; in addition, although obtained closed-form expressions are rather lengthy, for scattering directions lying within the incidence plane they support the physical interpretation of the scattering process, see Section III-D.

We have shown that the results obtained by our BA-PTSM are generally in good agreement with those obtained by the more refined, but much more computationally demanding, SSA-2 model, and they are always closer to the SSA-2 than to the SSA-1 results. Finally, we have presented a wide set of graphs and examples, in order to provide a first analysis of the dependencies of the scattering behavior on the main scattering parameters.

We finally stress again that our formulation is completely in closed form and the whole set of plots shown in this article is obtained in a time of the order of minutes with a common laptop.

In conclusion, due to its computational efficiency, our method can be usefully employed when scattering must be computed several times, such as in implementing inversion methods for the retrieval of surface parameters. In addition, it can be employed to predict the performance of the upcoming bistatic and multistatic radar remote sensing missions.

APPENDIX A

In this appendix, we show how the expressions (26)–(28) can be derived. Although (24) and (25) are already available in literature, for the sake of completeness they are considered here, too.

All required expressions can be written in terms of scalar or vector products of the incident and scattered wave wavenumber unit vectors

$$\hat{\mathbf{k}}_i = \sin \vartheta_i \hat{\mathbf{i}}_x - \cos \vartheta_i \hat{\mathbf{i}}_z \quad (47)$$

$$\hat{\mathbf{k}}_s = \sin \vartheta_s \cos \varphi_s \hat{\mathbf{i}}_x + \sin \vartheta_s \sin \varphi_s \hat{\mathbf{i}}_y + \cos \vartheta_s \hat{\mathbf{i}}_z \quad (48)$$

and of the normal unit vector of the tilted facet

$$\hat{\mathbf{n}}_l = \frac{-s_x \hat{\mathbf{i}}_x - s_y \hat{\mathbf{i}}_y + \hat{\mathbf{i}}_z}{\sqrt{1 + s_x^2 + s_y^2}}. \quad (49)$$

Hence, we obtain (50)–(54), as shown at the top of the next page.

In (51), (53), and (54), we have used the following relations:

$$\hat{\mathbf{i}}_z \times \hat{\mathbf{k}}_i = \sin \vartheta_i \hat{\mathbf{i}}_y \quad (55)$$

$$\hat{\mathbf{i}}_z \times \hat{\mathbf{k}}_s = -\sin \vartheta_s \sin \varphi_s \hat{\mathbf{i}}_x + \sin \vartheta_s \cos \varphi_s \hat{\mathbf{i}}_y \quad (56)$$

$$\hat{\mathbf{n}}_l \times \hat{\mathbf{k}}_i = s_y \cos \vartheta_i \hat{\mathbf{i}}_x + (\sin \vartheta_i - s_x \cos \vartheta_i) \hat{\mathbf{i}}_y + s_y \sin \vartheta_i \hat{\mathbf{i}}_z \quad (57)$$

$$\begin{aligned} \hat{\mathbf{n}}_l \times \hat{\mathbf{k}}_s = & -(s_y \cos \vartheta_s + \sin \vartheta_s \sin \varphi_s) \hat{\mathbf{i}}_x \\ & + (\sin \vartheta_s \cos \varphi_s + s_x \cos \vartheta_s) \hat{\mathbf{i}}_y \\ & + (-s_x \sin \vartheta_s \sin \varphi_s + s_y \sin \vartheta_s \cos \varphi_s) \hat{\mathbf{i}}_z. \end{aligned} \quad (58)$$

APPENDIX B

In this appendix, we provide guidelines for the analytical evaluation of expansion coefficients in (31) and, hence, of (29). In addition, we show how in-plane expressions (34) are obtained. To this end, it is useful to note that the tilted-facet polarimetric covariance matrix elements in (20) can be expressed as combinations of terms of the kind $\Theta_{pq,rs}(\vartheta_{li}, \vartheta_{ls}, \varphi_{ls}) \Phi(\varphi_l) \mathbf{B}_n(\beta_i) \mathbf{B}_m(\beta_s)$, where

$$\begin{aligned} \Theta_{pq,rs}(\vartheta_{li}, \vartheta_{ls}, \varphi_{ls}) = & \frac{4}{\pi} k^4 \cos^2 \vartheta_{li} \cos^2 \vartheta_{ls} F_{pq}(\vartheta_{li}, \vartheta_{ls}, \varphi_{ls}) \\ & \times F_{rs}^*(\vartheta_{li}, \vartheta_{ls}, \varphi_{ls}) W(\kappa_l) \end{aligned} \quad (59)$$

$$\Phi(\varphi_l) = 1 + \Delta \cos[2(\varphi_0 - \varphi_l)] \quad (60)$$

$$\text{and } \mathbf{B}_n(\beta_{i,s}) = \cos^{2-n} \beta_{i,s} \sin^n \beta_{i,s} \quad (61)$$

with n and m integers and $0 \leq n \leq 2$ and $0 \leq m \leq 2$.

Taylor power series expansion of the covariance matrix elements in (20) with respect to s_x and s_y can be readily obtained once expansions of $\Theta_{pq,rs}(\vartheta_{li}, \vartheta_{ls}, \varphi_{ls})$, $\Phi(\varphi_l)$, and $\mathbf{B}_n(\beta_{i,s})$ are performed.

The series expansion of $\Theta_{pq,rs}(\vartheta_{li}, \vartheta_{ls}, \varphi_{ls})$ up to the second order can be expressed, in the general case, as

$$\begin{aligned} \Theta_{pq,rs}(\vartheta_{li}, \vartheta_{ls}, \varphi_{ls}) & \cong C_{0,0}^{pq,rs} + C_{1,0}^{pq,rs} s_x + C_{0,1}^{pq,rs} s_y + C_{2,0}^{pq,rs} s_x^2 \\ & + C_{0,2}^{pq,rs} s_y^2 + C_{1,1}^{pq,rs} s_x s_y \end{aligned} \quad (62)$$

where expansion coefficients are defined in (35). The derivatives in (35) can be computed by applying the chain rule to (59) and (24), (26), and (27). This is particularly useful if we consider the in-plane scattering case, i.e., $\varphi_s = n\pi$, with $n = 0, 1$. In fact, it is easy to recognize that in this case

$$\begin{aligned} \left. \frac{\partial \cos \vartheta_{li,ls}}{\partial s_y} \right|_{s_x=s_y=0} & = \left. \frac{\partial^2 \cos \vartheta_{li,ls}}{\partial s_x \partial s_y} \right|_{s_x=s_y=0} = \left. \frac{\partial \cos \varphi_{ls}}{\partial s_{x,y}} \right|_{s_x=s_y=0} \\ & = \left. \frac{\partial^2 \cos \varphi_{ls}}{\partial s_x \partial s_y} \right|_{s_x=s_y=0} = 0 \end{aligned} \quad (63)$$

and

$$\sin \varphi_{ls} \Big|_{s_x=s_y=0} = \left. \frac{\partial \sin \varphi_{ls}}{\partial s_x} \right|_{s_x=s_y=0} = \left. \frac{\partial^2 \sin \varphi_{ls}}{\partial s_{x,y}^2} \right|_{s_x=s_y=0} = 0 \quad (64)$$

so that terms containing two co-polar Bragg coefficients, i.e., $p = q$ and $r = s$, can be expressed as

$$\Theta_{pp,rr}(\vartheta_{li}, \vartheta_{ls}, \varphi_{ls}) \cong C_{0,0}^{pp,rr} + C_{1,0}^{pp,rr} s_x + C_{2,0}^{pp,rr} s_x^2 + C_{0,2}^{pp,rr} s_y^2, \quad (65)$$

those containing one co-polar and one cross-polar Bragg coefficients, i.e., $p = q$ and $r \neq s$ or vice versa, as

$$\Theta_{pq,rs}(\vartheta_{li}, \vartheta_{ls}, \varphi_{ls}) \cong C_{0,1}^{pq,rs} s_y + C_{1,1}^{pq,rs} s_x s_y, \quad (66)$$

and those containing two cross-polar Bragg coefficients, i.e., $p \neq q$ and $r \neq s$, as

$$\Theta_{pq,rs}(\vartheta_{li}, \vartheta_{ls}, \varphi_{ls}) \cong C_{0,2}^{pq,rs} s_y^2. \quad (67)$$

With regard to $\Phi(\varphi_l)$, we assume that its first-order series expansion is sufficient, because second-order terms include a factor Δ that is usually much smaller than unity (see Section II), so that they can be neglected. We, therefore, obtain

$$\begin{aligned} \Phi(\varphi_l) \cong & 1 + \Delta \cos 2\varphi_w - 2\Delta \sin 2\varphi_w \\ & \times \left(\frac{\partial(\varphi_0 - \varphi_l)}{\partial s_x} \Big|_{s_x=s_y=0} s_x + \frac{\partial(\varphi_0 - \varphi_l)}{\partial s_y} \Big|_{s_x=s_y=0} s_y \right). \end{aligned} \quad (68)$$

The terms involving the first derivatives of $\varphi_0 - \varphi_l$ are canceled by the average operation, so that their expressions are of no concern here.

Finally, by using (25) and (28), and recalling that

$$\sin \beta = \frac{\tan \beta}{\sqrt{1 + \tan^2 \beta}} \quad (69)$$

we obtain the following second order expansion of $\mathbf{B}_n(\beta_{i,s})$:

$$\mathbf{B}_n(\beta_{i,s}) \cong \begin{cases} 1 - \frac{(s_x \sin \varphi_{i,s} - s_y \cos \varphi_{i,s})^2}{\sin^2 \vartheta_{i,s}} & \text{for } n = 0 \\ \frac{(s_x \sin \varphi_{i,s} - s_y \cos \varphi_{i,s})}{\sin \vartheta_{i,s}} \left(1 - \frac{s_x \cos \varphi_{i,s}}{\tan \vartheta_{i,s}} - \frac{s_y \sin \varphi_{i,s}}{\sin \vartheta_{i,s}} \right) & \text{for } n = 1 \\ \frac{(s_x \sin \varphi_{i,s} - s_y \cos \varphi_{i,s})^2}{\sin^2 \vartheta_{i,s}} & \text{for } n = 2 \end{cases} \quad (70)$$

with $\varphi_i = \pi$, and $\mathbf{B}_n(\beta_i) \mathbf{B}_m(\beta_s) \cong 0$ for $n + m > 2$.

By using (62), (67), and (70) in (20), and discarding terms of order higher than two, after some algebra we can obtain the coefficients of (29). In the in-plane scattering case, the use of (65)–(66), (67), and (70) in (20) leads to the covariance matrix elements in (34).

We finally note that expansions in (70) do not hold for small values of $\vartheta_{i,s}$, when $\sin \vartheta_{i,s}$ is of the order of $\sigma_{x,y}$ or smaller. Therefore, in all the plots presented in this work, the second-order terms of the expansions are suppressed for such small values of ϑ_s .

$$\cos \vartheta_{ii} = -\hat{\mathbf{n}}_l \cdot \hat{\mathbf{k}}_i = \frac{\cos \vartheta_i + s_x \sin \vartheta_i}{\sqrt{1 + s_x^2 + s_y^2}} \quad (50)$$

$$\begin{aligned} \tan \beta_i &= \sqrt{\frac{1 - \cos^2 \beta_i}{\cos^2 \beta_i}} = \sqrt{\frac{|\hat{\mathbf{n}}_l \times \hat{\mathbf{k}}_i|^2 - (\hat{\mathbf{i}}_y \cdot \hat{\mathbf{n}}_l \times \hat{\mathbf{k}}_i)^2}{(\hat{\mathbf{i}}_y \cdot \hat{\mathbf{n}}_l \times \hat{\mathbf{k}}_i)^2}} \\ &= \sqrt{\frac{(\hat{\mathbf{i}}_x \cdot \hat{\mathbf{n}}_l \times \hat{\mathbf{k}}_i)^2 + (\hat{\mathbf{i}}_z \cdot \hat{\mathbf{n}}_l \times \hat{\mathbf{k}}_i)^2}{(\hat{\mathbf{i}}_y \cdot \hat{\mathbf{n}}_l \times \hat{\mathbf{k}}_i)^2}} \\ &= \frac{s_y}{\sin \vartheta_i - s_x \cos \vartheta_i} \end{aligned} \quad (51)$$

$$\begin{aligned} \cos \vartheta_{ls} &= \frac{\hat{\mathbf{n}}_l \cdot \hat{\mathbf{k}}_s}{\cos \vartheta_s - s_x \sin \vartheta_s \cos \varphi_s - s_y \sin \vartheta_s \sin \varphi_s} \\ &= \frac{1}{\sqrt{1 + s_x^2 + s_y^2}} \end{aligned} \quad (52)$$

$$\begin{aligned} \cos \varphi_{ls} &= \frac{(\hat{\mathbf{n}}_l \times \hat{\mathbf{k}}_i) \cdot (\hat{\mathbf{n}}_l \times \hat{\mathbf{k}}_s)}{|\hat{\mathbf{n}}_l \times \hat{\mathbf{k}}_i| |\hat{\mathbf{n}}_l \times \hat{\mathbf{k}}_s|} = \frac{1}{\sqrt{(\sin \vartheta_i - s_x \cos \vartheta_i)^2 + s_y^2}} \\ &\quad \times \left(\frac{(\sin \vartheta_i - s_x \cos \vartheta_i)(\sin \vartheta_s \cos \varphi_s + s_x \cos \vartheta_s)}{\sqrt{(\sin \vartheta_s \cos \varphi_s + s_x \cos \vartheta_s)^2 + (-s_y \cos \vartheta_s - \sin \vartheta_s \sin \varphi_s)^2 + (-s_x \sin \vartheta_s \sin \varphi_s + s_y \sin \vartheta_s \cos \varphi_s)^2}} + \right. \\ &\quad \left. + \frac{s_y \cos \vartheta_i (-s_y \cos \vartheta_s - \sin \vartheta_s \sin \varphi_s) + s_y \sin \vartheta_i (-s_x \sin \vartheta_s \sin \varphi_s + s_y \sin \vartheta_s \cos \varphi_s)}{\sqrt{(\sin \vartheta_s \cos \varphi_s + s_x \cos \vartheta_s)^2 + (-s_y \cos \vartheta_s - \sin \vartheta_s \sin \varphi_s)^2 + (-s_x \sin \vartheta_s \sin \varphi_s + s_y \sin \vartheta_s \cos \varphi_s)^2}} \right) \end{aligned} \quad (53)$$

$$\begin{aligned} \tan \beta_s &= \sqrt{\frac{1 - \cos^2 \beta_s}{\cos^2 \beta_s}} = \sqrt{\frac{|\hat{\mathbf{i}}_z \times \hat{\mathbf{k}}_s|^2 |\hat{\mathbf{n}}_l \times \hat{\mathbf{k}}_i|^2 - (\hat{\mathbf{i}}_z \times \hat{\mathbf{k}}_s \cdot \hat{\mathbf{n}}_l \times \hat{\mathbf{k}}_i)^2}{(\hat{\mathbf{i}}_z \times \hat{\mathbf{k}}_s \cdot \hat{\mathbf{n}}_l \times \hat{\mathbf{k}}_i)^2}} \\ &= \frac{s_x \sin \varphi_s - s_y \cos \varphi_s}{\sin \vartheta_s + s_x \cos \vartheta_s \cos \varphi_s + s_y \cos \vartheta_s \sin \varphi_s} \end{aligned} \quad (54)$$

REFERENCES

- [1] M. Cherniakov, Ed., *Bistatic Radar: Emerging Technology*. Hoboken, NJ, USA: Wiley, 2008.
- [2] M. Rodriguez-Cassola, S. V. Baumgartner, G. Krieger, and A. Moreira, "Bistatic TerraSAR-X/F-SAR spaceborne-airborne SAR experiment: Description, data processing and results," *IEEE Trans. Geosci. Remote Sens.*, vol. 48, no. 2, pp. 781–794, Feb. 2010.
- [3] M. Rodriguez-Cassola *et al.*, "First bistatic spaceborne SAR experiments with TanDEM-X," *IEEE Geosci. Remote Sens. Lett.*, vol. 9, no. 1, pp. 33–37, Jan. 2012.
- [4] A. Moreira *et al.*, "Tandem-L: A highly innovative bistatic SAR mission for global observation of dynamic processes on the Earth's surface," *IEEE Geosci. Remote Sens. Mag.*, vol. 3, no. 2, pp. 8–23, Jun. 2015.
- [5] D. Comite and N. Pierdicca, "Bistatic radar systems at large baselines for ocean observation," *IEEE Trans. Geosci. Remote Sens.*, vol. 56, no. 3, pp. 1816–1828, Mar. 2018.
- [6] F. Daout, F. Schmitt, G. Ginolhac, and P. Fargette, "Multistatic and multiple frequency imaging resolution analysis-application to GPS-based multistatic radar," *IEEE Trans. Aerosp. Electron. Syst.*, vol. 48, no. 4, pp. 3042–3057, Oct. 2012.
- [7] M. Antoniou, Z. Zeng, L. Feifeng, and M. Cherniakov, "Experimental demonstration of passive BSAR imaging using navigation satellites and a fixed receiver," *IEEE Geosci. Remote Sens. Lett.*, vol. 9, no. 3, pp. 477–481, May 2012.
- [8] T. Zeng *et al.*, "Multiangle BSAR imaging based on BeiDou-2 navigation satellite system: Experiments and preliminary results," *IEEE Trans. Geosci. Remote Sens.*, vol. 53, no. 10, pp. 5760–5773, Oct. 2015.
- [9] F. Santi, M. Antoniou, and D. Pastina, "Point spread function analysis for GNSS-based multistatic SAR," *IEEE Geosci. Remote Sens. Lett.*, vol. 12, no. 2, pp. 304–308, Feb. 2015.
- [10] C. S. Ruf *et al.*, "A new paradigm in Earth environmental monitoring with the CYGNSS small satellite constellation," *Sci. Rep.*, vol. 8, no. 1, Jun. 2018, Art. no. 8782.
- [11] V. U. Zavorotny, S. Gleason, E. Cardellach, and A. Camps, "Tutorial on remote sensing using GNSS bistatic radar of opportunity," *IEEE Geosci. Remote Sens. Mag.*, vol. 2, no. 4, pp. 8–45, Dec. 2014.
- [12] N. Pierdicca, L. Pulvirenti, F. Ticconi, and M. Brogioni, "Radar bistatic configurations for soil moisture retrieval: A simulation study," *IEEE Trans. Geosci. Remote Sens.*, vol. 46, no. 10, pp. 3252–3264, Oct. 2008.
- [13] M. P. Clarizia, C. S. Ruf, P. Jales, and C. Gommenginger, "Spaceborne GNSS-R minimum variance wind speed estimator," *IEEE Trans. Geosci. Remote Sens.*, vol. 52, no. 11, pp. 6829–6843, Nov. 2014.
- [14] J. T. Johnson and J. D. Ouellette, "Polarization features in bistatic scattering from rough surfaces," *IEEE Trans. Geosci. Remote Sens.*, vol. 52, no. 3, pp. 1616–1626, Mar. 2014.
- [15] J.-S. Lee and E. Pottier, *Polarimetric Radar Imaging: From Basics to Applications*. Boca Raton, FL, USA: CRC Press, 2009.
- [16] J. Wright, "A new model for sea clutter," *IEEE Trans. Antennas Propag.*, vol. AP-16, no. 2, pp. 217–223, Mar. 1968.
- [17] G. R. Valenzuela, "Scattering of electromagnetic waves from a tilted slightly rough surface," *Radio Sci.*, vol. 3, no. 11, pp. 1057–1066, Nov. 1968.
- [18] A. Voronovich, "Small-slope approximation for electromagnetic wave scattering at a rough interface of two dielectric half-spaces," *Waves Random Media*, vol. 4, no. 3, pp. 337–367, Jul. 1994.
- [19] S. H. Yueh, "Modeling of wind direction signals in polarimetric sea surface brightness temperatures," *IEEE Trans. Geosci. Remote Sens.*, vol. 35, no. 6, pp. 1400–1418, Nov. 1997.
- [20] C. Zuffada, A. K. Fung, J. Parker, M. Okolicanyi, and E. Huang, "Polarization properties of the GPS signal scattered off a wind driven ocean," *IEEE Trans. Antennas Propag.*, vol. 52, no. 1, pp. 172–187, Jan. 2004.
- [21] T. M. Elfouhaily and C.-A. Guérin, "A critical survey of approximate scattering wave theories from random rough surfaces," *Waves Random Media*, vol. 14, no. 4, pp. R1–R40, Oct. 2004.
- [22] J. T. Johnson and T. M. Elfouhaily, "Computation of oceanlike surface thermal emission and bistatic scattering with the reduced local curvature approximation," *IEEE Trans. Geosci. Remote Sens.*, vol. 45, no. 7, pp. 2108–2115, Jul. 2007.

- [23] A. Arnold-Bos, A. Khenchaf, and A. Martin, "Bistatic radar imaging of the marine environment—Part I: Theoretical background," *IEEE Trans. Geosci. Remote Sens.*, vol. 45, no. 11, pp. 3372–3383, Nov. 2007.
- [24] G. Soriano and C.-A. Guérin, "A cutoff invariant two-scale model in electromagnetic scattering from sea surfaces," *IEEE Geosci. Remote Sens. Lett.*, vol. 5, no. 2, pp. 199–203, Apr. 2008.
- [25] A. Iodice, A. Natale, and D. Riccio, "Retrieval of soil surface parameters via a polarimetric two-scale model," *IEEE Trans. Geosci. Remote Sens.*, vol. 49, no. 7, pp. 2531–2547, Jul. 2011.
- [26] A. G. Voronovich and V. U. Zavorotny, "Full-polarization modeling of monostatic and bistatic radar scattering from a rough sea surface," *IEEE Trans. Antennas Propag.*, vol. 62, no. 3, pp. 1362–1371, Mar. 2014.
- [27] G. Di Martino, A. Iodice, A. Natale, and D. Riccio, "Polarimetric two-scale two-component model for the retrieval of soil moisture under moderate vegetation via L-band SAR data," *IEEE Trans. Geosci. Remote Sens.*, vol. 54, no. 4, pp. 2470–2491, Apr. 2016.
- [28] G. Di Martino, A. Iodice, and D. Riccio, "Closed-form anisotropic polarimetric two-scale model for fast evaluation of sea surface backscattering," *IEEE Trans. Geosci. Remote Sens.*, vol. 57, no. 8, pp. 6182–6194, Aug. 2019.
- [29] D. Comite and N. Pierdicca, "Monostatic and bistatic scattering modeling of the anisotropic rough soil," *IEEE Trans. Geosci. Remote Sens.*, vol. 57, no. 5, pp. 2543–2556, May 2019.
- [30] S. H. Yueh, W. J. Wilson, and S. Dinardo, "Polarimetric radar remote sensing of ocean surface wind," *IEEE Trans. Geosci. Remote Sens.*, vol. 40, no. 4, pp. 793–800, Apr. 2002.
- [31] A. Khenchaf, "Bistatic scattering and depolarization by randomly rough surfaces: Application to the natural rough surfaces in X-band," *Waves Random Media*, vol. 11, no. 2, pp. 61–89, Apr. 2001.
- [32] A. Awada, M. Y. Ayari, A. Khenchaf, and A. Coatanhay, "Bistatic scattering from an anisotropic sea surface: Numerical comparison between the first-order SSA and the TSM models," *Waves Random Complex Media*, vol. 16, no. 3, pp. 383–394, Aug. 2006.
- [33] X. Blaes and P. Defourny, "Characterizing bidimensional roughness of agricultural soil surfaces for SAR modeling," *IEEE Trans. Geosci. Remote Sens.*, vol. 46, no. 12, pp. 4050–4061, Dec. 2008.
- [34] T. Elfouhaily, B. Chapron, K. Katsaros, and D. Vandemark, "A unified directional spectrum for long and short wind-driven waves," *J. Geophys. Res. Oceans*, vol. 102, no. C7, pp. 15781–15796, Jul. 1997.
- [35] C. S. Cox and W. Munk, "Measurement of the roughness of the sea surface from photographs of the sun's glitter," *J. Opt. Soc. Amer.*, vol. 44, pp. 838–850, 1954.
- [36] S. J. Katzberg, O. Torres, and G. Ganoe, "Calibration of reflected GPS for tropical storm wind speed retrievals," *Geophys. Res. Lett.*, vol. 33, no. 18, p. L18602, 2006.
- [37] G. Franceschetti, A. Iodice, and D. Riccio, "Fractal models for scattering from natural surfaces," in *Scattering*, R. Pike and P. Sabatier Eds., London, U.K.: Academic, 2001, pp. 467–485.
- [38] F. T. Ulaby, R. K. Moore, and A. K. Fung, *Microwave Remote Sensing*, vol. 2. Reading, MA, USA: Artech House, 1982.
- [39] W. Fuscaldo, A. Di Simone, L. M. Millefiori, A. Iodice, P. Braca, and P. K. Willett, "A convenient analytical framework for electromagnetic scattering from composite targets," *Radio Sci.*, vol. 54, no. 8, pp. 785–807, Aug. 2019.
- [40] A. Di Simone *et al.*, "Analytical models for the electromagnetic scattering from isolated targets in bistatic configuration: Geometrical optics solution," *IEEE Trans. Geosci. Remote Sens.*, vol. 58, no. 2, pp. 861–880, Feb. 2020.
- [41] J.-S. Lee, D. L. Schuler, and T. L. Ainsworth, "Polarimetric SAR data compensation for terrain azimuth slope variation," *IEEE Trans. Geosci. Remote Sens.*, vol. 38, no. 5, pp. 2153–2163, Sep. 2000.
- [42] *Wolfram Mathematica*. Accessed: Apr. 14, 2020. [Online]. Available: <https://reference.wolfram.com/language/guide/Calculus.html>
- [43] *MathWorks*. Accessed: Apr. 14, 2020. [Online]. Available: <https://it.mathworks.com/help/symbolic/calculus.html>
- [44] G. Di Martino, A. Iodice, D. Poreh, and D. Riccio, "Pol-SARAS: A fully polarimetric SAR raw signal simulator for extended soil surfaces," *IEEE Trans. Geosci. Remote Sens.*, vol. 56, no. 4, pp. 2233–2247, Apr. 2018.
- [45] P. W. Vachon and J. Wolfe, "C-band cross-polarization wind speed retrieval," *IEEE Geosci. Remote Sens. Lett.*, vol. 8, no. 3, pp. 456–459, May 2011.
- [46] W. Dierking, "Quantitative roughness characterization of geological surfaces and implications for radar signature analysis," *IEEE Trans. Geosci. Remote Sens.*, vol. 37, no. 5, pp. 2397–2412, Sep. 1999.
- [47] G. Di Martino, A. Iodice, D. Riccio, and G. Ruello, "Equivalent number of scatterers for SAR speckle modeling," *IEEE Trans. Geosci. Remote Sens.*, vol. 52, no. 5, pp. 2555–2564, May 2014.



Gerardo Di Martino (Senior Member, IEEE) was born in Naples, Italy, in 1979. He received the Laurea degree (*cum laude*) in telecommunication engineering and the Ph.D. degree in electronic and telecommunication engineering from the University of Naples Federico II, Naples, in 2005 and 2009, respectively.

From 2009 to 2016, he was with the University of Naples Federico II, where he was involved in projects regarding applied electromagnetics and remote sensing topics. From 2014 to 2016, he was also with the Italian National Consortium for Telecommunications, Parma, Italy, and with Regional Center Information Communication Technology, Naples. He is a Tenure-Track Assistant Professor of electromagnetics with the Department of Electrical Engineering and Information Technology, University of Naples Federico II. His main research interests include microwave remote sensing and electromagnetics, with a focus on electromagnetic scattering from natural surfaces and urban areas, synthetic aperture radar (SAR) signal processing and simulation, information retrieval from SAR data, and electromagnetic propagation in urban areas.

Dr. Di Martino is an Associate Editor of the IEEE ACCESS and a Section Editorial Board Member of the *Remote Sensing* (MDPI).



Alessio Di Simone (Member, IEEE) was born in Torre del Greco, Italy, in 1989. He received the B.Sc. and M.Sc. Laurea degrees (*cum laude*) in telecommunication engineering and the Ph.D. degree in information technology and electrical engineering from the University of Naples Federico II, Naples, Italy, in 2011, 2013, and 2017, respectively.

In 2016, he joined the Universitat Politècnica de Catalunya, Barcelona, Spain, as a Visiting Researcher. In 2017 and 2018, he joined the Centre for Maritime Research and Experimentation (CMRE), NATO Science and Technology Organization, La Spezia, Italy, as a Visiting Researcher. Since 2017, he has been a Research Fellow with the Department of Information Technology and Electrical Engineering, University of Naples Federico II. His main research interests are in the field of microwave remote sensing and electromagnetics including modeling of the electromagnetic scattering from natural surfaces, urban areas, and artificial targets, and simulation and processing of synthetic aperture radar (SAR) and GNSS-R data.

Dr. Di Simone was awarded a prize for the Best Master Thesis in Remote Sensing by the IEEE South Italy Geoscience and Remote Sensing Chapter in 2015.



Antonio Iodice (Senior Member, IEEE) was born in Naples, Italy, in 1968. He received the Laurea degree (*cum laude*) in electronic engineering and the Ph.D. degree in electronic engineering and computer science, from the University of Naples Federico II, Naples, in 1993 and 1999, respectively.

In 1995, he joined the Research Institute for Electromagnetism and Electronic Components, Italian National Council of Research (IRECE-CNR), Naples. From 1999 to 2000, he was with Telespazio S.p.A., Rome, Italy. He was a Research Scientist

with the University of Naples Federico II from 2000 to 2004 and an Associate Professor of electromagnetics from 2005 to 2018. He is currently a Full Professor of electromagnetics with the Department of Electrical Engineering and Information Technology, University of Naples Federico II. He has been involved as a Principal Investigator or a Co-Investigator in several projects funded by the European Union (EU), Italian Space Agency (ASI), Italian Ministry of Education and Research (MIUR), Campania Regional Government, and private companies. He has authored or co-authored over 300 articles, of which over 90 published on refereed journals. His main research interests are in the field of microwave remote sensing and electromagnetics: modeling of electromagnetic scattering from natural surfaces and urban areas, simulation and processing of synthetic aperture radar (SAR) signals, and electromagnetic propagation in urban areas.

Prof. Iodice received the “2009 Sergei A. Schelkunoff Transactions Prize Paper Award” from the IEEE Antennas and Propagation Society for the best paper published in 2008 on the IEEE TRANSACTIONS ON ANTENNAS AND PROPAGATION. He was recognized as a 2015 Best Reviewer for the IEEE TRANSACTIONS ON GEOSCIENCE AND REMOTE SENSING by the IEEE Geoscience and Remote Sensing Society. He is the Chair of the IEEE South Italy Geoscience and Remote Sensing Chapter.



Daniele Riccio (Fellow, IEEE) was born in Naples, Italy. He received the Laurea degree (*cum laude*) in electronic engineering from the University of Naples Federico II, Naples, in 1989.

His career has been developing at the University of Naples Federico II, where he is a Full Professor of electromagnetic fields with the Department of Electrical Engineering and Information Technology. He was also a Research Scientist with the Institute for Research on Electromagnetics and Electronic Components, Italian National Research Council, Naples, from 1989 to 1994, a Guest Scientist with German Aerospace Centre (DLR), Munich, Germany, from 1994 to 1995, and a Research Affiliate with NASA, USA from 2010 to 2018. He taught abroad as a Lecturer to the Ph.D. Programme with the Universitat Politècnica de Catalunya, Barcelona, Spain, in 2006 and with Czech Technical University, Prague, Czech Republic, in 2012. He is a member of Cassini Radar Science Team. He is the Coordinator of the Ph.D. Schools in Information and Communication Technology for Health and in Information Technology and Electrical Engineering, University of Napoli Federico II as well as a Board member for the Ph.D. Programme on Space at the Scuola Superiore Meridionale, Naples. He has authored three books, including *Scattering, Natural Surfaces, and Fractals* (2007) and over 450 scientific articles. His research interests include remote sensing, electromagnetic scattering from complex media and surfaces, synthetic aperture radar techniques, application of fractal geometry to remote sensing, and propagation of electromagnetic fields for wireless communication networks planning.

Prof. Riccio is the Athenaeum Representative within the Assembly of the National Inter-University Consortium for Telecommunications (CNIT) and of the Italian Society of Electromagnetism (SIEm). He has been elected as Board Member of CNIT and SIEm, where he has also been appointed Secretary. He was a recipient of the 2009 Sergei A. Schelkunoff Transactions Prize Paper Award for the best paper published in 2008 on the IEEE TRANSACTIONS ON ANTENNAS AND PROPAGATION. He serves as an Associate Editor for some journals on *Remote Sensing*. He was the General Chair of the 5G International PhD School in 2018 and 2019.